Low cycle fatigue modelling of cellular materials produced by laser-powder bed fusion

Marco Pelegatti [a,*], Denis Benasciutti [b], Francesco De Bona [a], Enrico Salvati [a]

[a] Polytechnic Department of Engineering and Architecture, University of Udine, via delle Scienze 208, 33100 Udine, Italy
[b] Department of Engineering, University of Ferrara, via Saragat 1, 44122 Ferrara, Italy

ABSTRACT

A finite element (FE) modelling approach is developed to reproduce the cyclic elastoplastic response and to assess the low cycle fatigue (LCF) life of two cellular materials (strut-based, gyroid) investigated in a previous experimental campaign. The cyclic response of different FE models (unit cell, one layer structure) is compared in terms of computational cost and modelling accuracy. The most satisfactory model is further updated based on the actual relative density of fabricated cellular materials. The LCF assessment exploits a volume-based strain energy density (SED) criterion, calibrated after comparing static properties of strut-based and bulk materials. The cyclic elastoplastic response is well reproduced for both cellular materials, whereas the estimated fatigue lives are in closer agreement for the gyroid structure than the strut-based one.

1. Introduction

Architected cellular materials, also known as cellular structures, can replace heavy bulk components with complex, engineered porous structures in order to reduce weight and optimise mechanical properties. This class of materials was conceived a few decades ago [1]. However, it was only with the spreading of additive manufacturing (AM) that many efforts were devoted to developing architected cellular materials [2]. The use of AM unlocked the ability to produce complex shapes at the micrometre scale with unprecedented accuracy and reproducibility. The topology of the unit cell, its periodic arrangement in the space and the porosity of the structure are intentionally designed to fulfil specific engineering functions, exploiting the advantages of the manufacturing process [3–6]. Energy or impact absorbers with a cellular structure core can achieve a high energy absorption-to-weight ratio, overcoming solutions where bulk pieces of materials are used [7]. Cellular materials were proved to provide a higher dissipation in vibration dampers thanks to the intricate geometry leading to internal friction at the beam joints [8]. Brackets in aerospace and automotive sectors can be lightened in slightly loaded areas of the component while simultaneously providing structural continuity and performance [9]. The architecture of cellular materials was also tailored to improve the durability of aerospace components subjected to thermo-mechanical loads, such as turbine blades [10].

The mechanical characterisation of cellular materials is crucial in many of the abovementioned applications, where the reliability against fatigue failure of the mechanical pieces is of foremost importance [9,11–13]. As it is well known, predicting the fatigue life of additively manufactured materials remains a challenge due to the influence of process-induced defects and surface roughness [14–17]. In the case of cellular materials, the problem becomes even more complicated. Besides the complex shape of the component at the macroscale, the intricate geometry of a single cell at the microscale poses a challenge in developing a modelling strategy. A level of modelling detail that constitutes a trade-off between complexity and computational effort is indeed required. Moreover, the cell size is usually comparable with the resolution of the AM process. This aspect can lead to significant differences in geometry and dimension between the as-built and as-designed structures, thus requiring the model to be further calibrated and improved based on experimental data. Finally, the structural integrity criterion to assess fatigue strength must be as general as possible and should be applied to any cell topology with smooth curved surfaces or sharp notches.

In the context of high cycle fatigue (HCF), several studies proposed different approaches to account for the abovementioned aspects. Among these works, a short selection is here summarised. A more comprehensive review study on fatigue assessment of cellular structures can be found in [18]. The modelling strategy adopted by Refai et al. [19]

* Corresponding author.
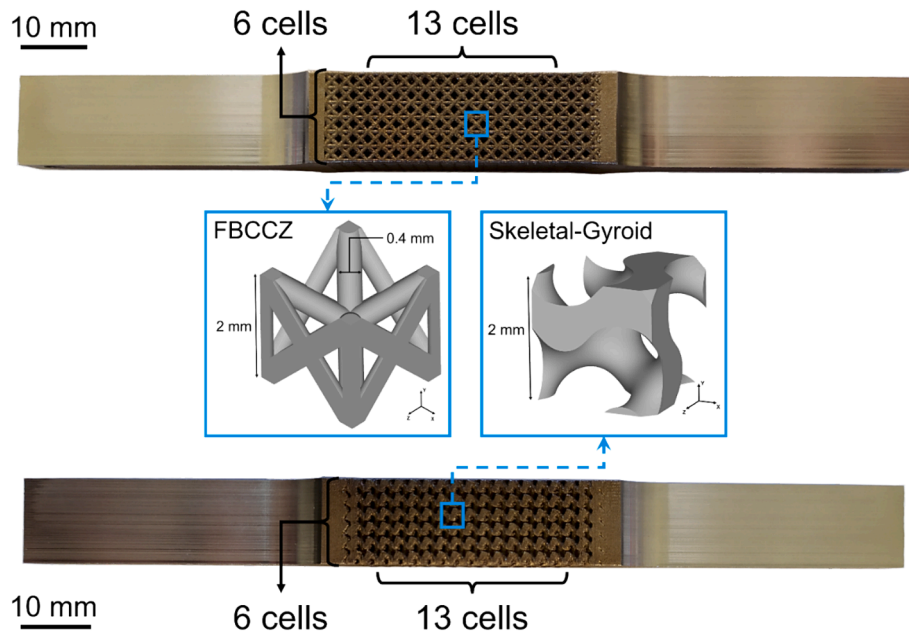 *E-mail address:* pelegatti.marco@spes.uniud.it (M. Pelegatti).

Fig.1. Cellular specimens and unit cell topologies: FBCCZ and skeletal-gyroid.

consists of estimating, with finite element (FE) models, the fatigue strength of various cell topologies by applying loads through periodic boundary conditions (PBCs) on unit cells. This approach assumes that the fatigue strength of the structure is derived from the fatigue strength of a single cell with periodicity conditions, neglecting the boundary effects on its mechanical behaviour. The numerical results were also corrected to include the influence of the surface roughness by modelling the geometry obtained by micro-Computed Tomography (μCT) scans. Finally, Crossland's criterion was adopted to consider stress multi-axiality. A different modelling strategy based on beam elements was used by Burr et al. [20] to discretise the lattice structure (i.e. cellular structures composed of struts and nodes). A random radius size was sampled from experimental statistic distributions and assigned for each beam element to account for the geometrical errors. A cascading failure-based model, inspired by Zargarian et al. [21,22], was implemented to retrieve the fatigue life of the specimens. In this approach, the failure of individual struts is estimated by using the axial stress and the Miner's damage rule. One of the drawbacks of this method is that the effect of stress concentrations near nodes and surface roughness are included empirically by using a corrective coefficient and a random S-N curve, respectively. Although beam elements are less computationally demanding, they cannot capture the local three-dimensional effects, such as stress concentrations and increased stiffness at the nodes.

Raghavendra et al. pursued a hybrid modelling strategy that combines the unit cell approach and beam element discretisation [23]. The lattice specimens were first discretised by beam elements. Then, the displacement field obtained at the boundaries of selected unit cells was used as boundary conditions for the 3D solid model through a sub-modelling procedure. The as-built geometry of the lattice specimens was analysed by μCT to update both the beam and 3D models. Finally, the fatigue strength was evaluated using an average strain energy density (SED) criterion. Simulating the response of the lattice structure using an equivalent homogeneous material, as done by Coluccia et al. [24], is yet another modelling strategy to reduce the computational effort. In fact, the architected cellular materials can often be considered equivalent homogeneous materials at the component level despite being structures. However, a fundamental condition in treating cellular structures as homogeneous materials is the length-scale separation between the representative volume element of the cellular structures (i.e. unit cell) and the component, which is not always satisfied. Unlike Refai

et al., the entire specimen was modelled, and the cell with the highest strain tensor norm was considered the most critical. A de-homogenisation process was applied to the critical cell, and eventually, Crossland's criterion was used to predict the fatigue failure of the specimen.

With respect to HCF, in the case of low cycle fatigue (LCF), the cyclic elastoplastic behaviour of the material has also to be considered. Therefore, new modelling strategies and structural integrity criteria are required. Nevertheless, studies dealing with cellular materials produced by AM are incredibly scarce. A methodology to assess the fatigue life in the LCF regime of two- and three-dimensional lattice structures was proposed by Molavitabrizi et al. [25], including plasticity and the influence of notches. Cyclic FE simulations were performed on unit cells using PBCs to reduce the computational cost. The theory of critical distance was applied using a critical surface area around the critical point and an equivalent strain range. Finally, Morrow and Manson-Coffin models were used to obtain the reversals to failure. The approach was applied to two cell topologies, and a comparison with experimental data from the literature is presented for a two-dimensional lattice structure produced by water-jetting. However, the main drawback of the proposed model is the need for experimental validation for three-dimensional cellular materials produced by AM. An analogous shortcoming is encountered in the work of Zhang et al. [26], where the cyclic elastoplastic behaviour of triply periodic minimal surface- (TPMS-)based cellular structures under compression-compression loading was simulated. A continuum damage model based on the plastic SED range was included in the simulations to monitor the failure process during cycling. Besides comparing the fatigue performance of the skeletal-diamond and skeletal-gyroid cells, the mentioned study provides some clues on the evolution of the stress–strain response due to the material softening and damage interaction. The number of cycles to crack initiation at different strain amplitudes was instead predicted by Mozafari et al. for a variety of strut- and TPMS-based cellular materials [27]. The numerical strategy is based on simulating the cyclic elastoplastic response of the unit cell subjected to compression-compression fatigue loading with PBCs. The plastic SED in a cycle is considered the damaging variable that accumulates until it reaches a critical value for the bulk material. Unfortunately, the modelling strategy was calibrated and validated for fatigue data in the HCF regime, whereas only numerical results are presented in the LCF region. A recent study by Doroszko and
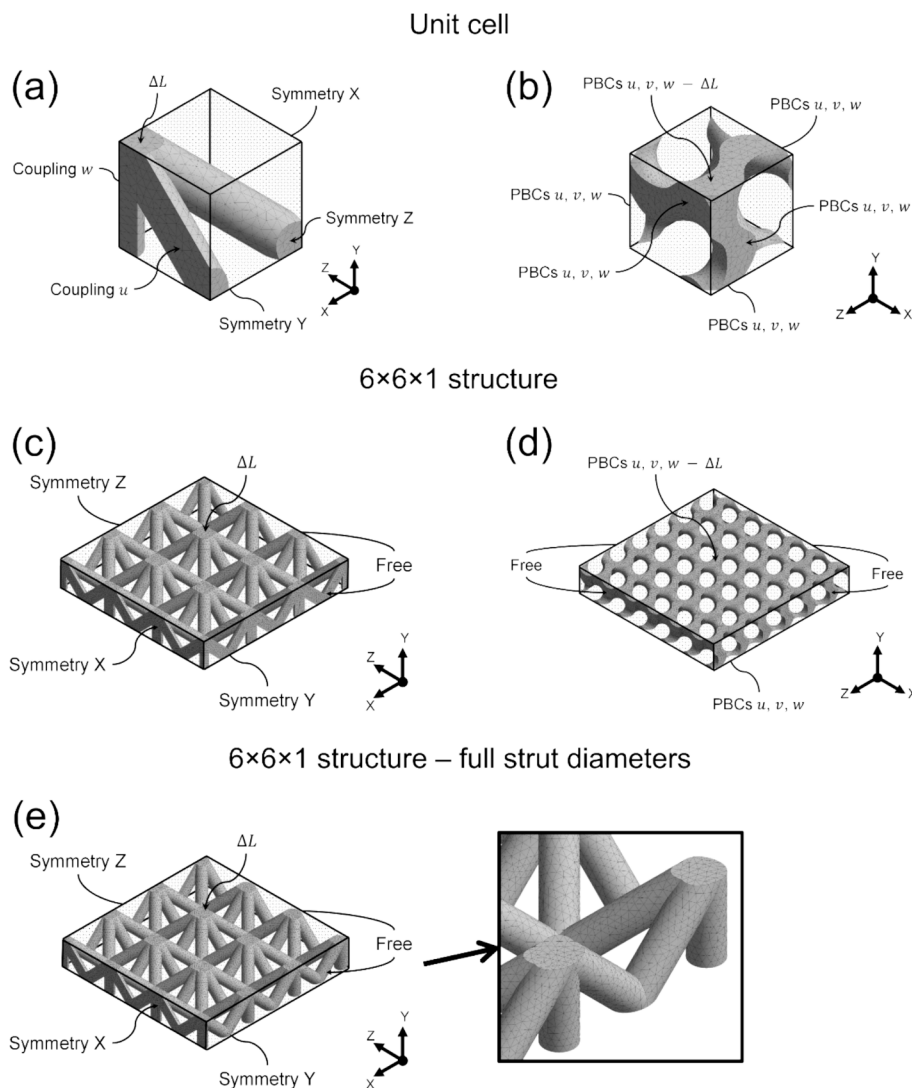
Unit cell

Fig. 2. Finite element models for the cellular materials using different levels of approximations: unit cell for (a) FBCCZ and (b) gyroid; 6×6×1 structure for (c) FBCCZ and (d) gyroid; (e) 6×6×1 structure with full strut diameters for FBCCZ (u, v and w are the displacements along X, Y and Z, respectively; PBCs – periodic boundary conditions).

Seweryn presented FE simulations of CT-reconstructed cellular structures to model the cyclic response and estimate the cycles to failure [28]. However, the investigated lifetime interval is limited to the HCF, where narrow macroscopic stress–strain hysteresis loops were recorded. Furthermore, the cellular material was loaded in stress control, unlike the typical LCF tests.

The abovementioned studies on LCF assessment proposed interesting approaches; nevertheless, their main weakness lies in a lack of direct experimental validation. Consequently, beyond the uncertainty on the validity of the fatigue strength criterion, a discussion on the cyclic elastoplastic response is needed. The current study aims to define a straightforward methodology for modelling the cyclic elastoplastic behaviour and predicting the LCF lifetime of cellular structures produced by AM, directly comparing it to the experimental data obtained in a previous study [29]. This methodology can serve as an engineering tool to assess the LCF performance of cellular materials with different architectures when employed in applications involving cyclic macroscopic plasticity, such as vibration dampers or turbine engine components. The article is structured in three main parts: the modelling strategy, the cyclic elastoplastic response and the fatigue life assessment. In the first part of the article, different modelling strategies based on a unit cell and a one-layer structure are compared. Two types of cellular

materials, a strut-based and a gyroid cell, are thoroughly investigated. A discussion on the boundary effects and the difference between the relative density of as-built and as-designed cellular specimens permit the FE models of the cellular structures to be defined. The simulated cyclic elastoplastic response is compared to the experimental data in the second part. Finally, a procedure for the fatigue assessment is developed in the third part. An attempt to extend the local average SED method from the HCF to the LCF regime is proposed to include the notch effect.

2. Cellular materials

The experimental data from LCF tests of cellular materials were collected in a recent publication by the authors of the present manuscript, Pelegatti et al. [29], where a strut-based and a TPMS-based cell were studied. The cellular specimens were produced by laser-powder bed fusion (L-PBF) – laser beam powder bed fusion of metals (PBF-LB/M) according to ISO/ASTM 52900:2021 – using 316L steel. The gauge part of the cellular specimens comprises 6×6×13 cells with a cell side equal to 2 mm, as schematised in Fig. 1. The strut-based unit cell, called FBCCZ, is composed of 28 struts and 13 joints. The TPMS-based is a skeletal-gyroid cell obtained from the gyroid minimal surface [4,30]. The as-designed relative density, i.e. the density of the cellular material

Table 1
Material parameters of the 316L steel produced by laser-powder bed fusion [34].

Elastic properties		Kinematic hardening						Isotropic hardening	
E(MPa)	$\sigma_{y,0}$(MPa)	C_1(MPa)	γ_1	C_2(MPa)	γ_2	C_3(MPa)	γ_3	R_∞(MPa)	b
194,323	380	320,000	5500	97,000	1000	25,000	150	−140	0.6128

divided by the density of the base material, of both the cellular structures is about 31 %. The relative density of the FBCCZ is ruled by the strut diameter equal to 0.4 mm, whereas the density of the skeletal-gyroid depends on the constant parameter of the gyroid *iso*-surface equation, usually indicated with the letter *t*, equal to −0.57 [31].

The LCF tests of cellular specimens were carried out in strain control using an axial clip-on extensometer. Different macroscopic strain amplitudes with zero mean strain were imposed for the two cellular materials: 0.3 %, 0.4 %, 0.5 % and 0.7 % for the FBCCZ, and 0.3 %, 0.5 %, 0.7 %, 1.0 % and 1.2 % for the gyroid. Several stress–strain hysteresis loops, as well as the maximum and minimum stresses and the number of cycles to failure, were recorded during the tests.

3. Modelling strategy

3.1. Geometry, boundary conditions and material constitutive model

The experimental cyclic behaviour of the cellular specimen could be accurately simulated by modelling the entire gauge part of the specimen with 6×6×13 cells. Unfortunately, this modelling strategy is unfeasible for a number of reasons related to the high computational effort required: the high number of elements necessary to discretise the specimen intricated geometry; the non-linearity of the material behaviour; the need to compute the specimen elastoplastic response for a large number of cycles in the LCF regime.

A trade-off between model complexity and computational effort has to be found, leading to a simplified model that still preserves accuracy. Two different strategies were pursued in the present study, as reported in Fig. 2. The first one consists of simulating the response of one unit cell subjected to PBCs along all three directions. The PBCs allow the response of a unit cell inside a periodic structure to be accurately reproduced. However, it is worth mentioning that the mechanical response obtained using the unit cell with PBCs becomes a reasonable approximation for cellular structures with a sufficiently high number of cells. In the second strategy, the geometry of a 6×6×1 cellular structure is considered, and the PBCs were set only along the loading direction, whereas the edges of the structure are free to move in the other two directions.

The modelling strategy for FBCCZ and gyroid cells is further differentiated. Since the FBCCZ unit cell has three planes of symmetry, an eight-quarter model can be exploited, as shown in Fig. 2 (a). This choice is acceptable if the PBCs can be approximated by imposing the faces of the cell to remain flat during deformation (without warping). Therefore, the nodes of the external faces are constrained to have the same displacement perpendicular to the face to which they belong. The symmetries of the FBCCZ structure can also be exploited in the case of the 6×6×1 FBCCZ model, where the nodes on the external faces are left unconstrained. Because the as-designed structure presents struts with full diameters at the boundaries, two model geometries of the 6×6×1 FBCCZ structure were also considered: one repeats the unit cell in the cross-section of the specimen, as depicted in Fig. 2 (c), whereas the other also includes the full diameter of the edge struts, see Fig. 2 (e).

The gyroid unit cell must be modelled entirely because the geometry does not show symmetry planes. Furthermore, the absence of symmetry planes and the specific distribution of the material within the cell leads to a warping of the external faces during the deformation. In this specific case, the PBCs cannot be approximated as done for the FBCCZ cell and must be imposed on each of the opposed faces of the cell. Concerning the 6×6×1 gyroid structure, all the cells must be modelled, and the PBCs

enforced along the loading direction. The unit cell and 6×6×1 gyroid geometries with the applied boundary conditions are illustrated in Fig. 2 (b, d). The PBCs were set by following the procedure proposed by Okereke et al. [32], and their implementation is described in Appendix A.

The material adopted in the FE model is the 316L steel produced by L-PBF that was investigated by the authors in previous works [33,34]. An elastoplastic material model with combined kinematic and isotropic hardening was used in the simulations to replicate the cyclic elastoplastic response of the cellular structures. Chaboche's model was adopted as the kinematic hardening model to reproduce the non-linear stress–strain response of the material during each cycle. The kinematic hardening variable is the back stress tensor $\boldsymbol{X}$, whose increment is governed by the following equation:

$$\mathrm{d}\boldsymbol{X} = \sum_{i=1}^{3} \frac{2}{3} C_i \mathrm{d}\boldsymbol{\varepsilon}_{pl} - \gamma_i \boldsymbol{X}_i \mathrm{d}p \tag{1}$$

where the parameter C_i is related to the plastic strain-hardening modulus of the material, whereas γ_i rules its decrease. The increment of the back stress tensor $\mathrm{d}\boldsymbol{X}$ depends on both the increment in the plastic strain tensor, $\mathrm{d}\boldsymbol{\varepsilon}_{pl}$, and the accumulated equivalent plastic strain, p.

The cyclic softening of the material was instead replicated using Voce's isotropic hardening model. The incremental form of the model is the following:

$$\mathrm{d}R = b(R_\infty - R)\mathrm{d}p \tag{2}$$

where R is the isotropic hardening variable. The parameter R_∞ represents the saturated value of R, and b is the speed of stabilisation, i.e. how fast the variable R reaches the value R_∞ with increasing p.

Interested readers can find more details on the constitutive model equations and the meaning of the parameters in the reference [35]. The values of the constitutive model parameters, listed in Table 1, were previously calibrated from experimental data obtained by testing bulk cylindrical specimens [34]. Briefly, the calibration consisted of fitting the cyclic elastoplastic response of the L-PBF 316L steel recorded during LCF tests. The stress–strain hysteresis loops were fitted using Chaboche's model expression for the uniaxial loading condition, whereas the cyclic stress response (i.e. cyclic softening) was fitted by Voce's model. The elastic properties refer to Young's modulus E and the initial yield stress $\sigma_{y,0}$.

The FE simulations were performed with the small deformation assumption except for the tensile test simulation of the FBCCZ, discussed in Section 5.2, where the large displacements option was enabled.

The FE simulations were carried out using the commercial code Ansys®, and the geometries were discretised by 10-node tetrahedral elements (SOLID187). Within the element, the displacement field is quadratic, and the stress/strain fields are linear. The mean size of the elements was obtained by a mesh convergence study on the global response of a single unit cell subjected to a monotonic displacement load, where the control variable was the reaction force. A mean element size of 0.083 mm was selected for the FBBCZ cell and 0.078 mm for the gyroid. The mesh was then slightly refined at notches for the fatigue assessment using the local average SED. Specifically, a refinement was necessary around the critical point.
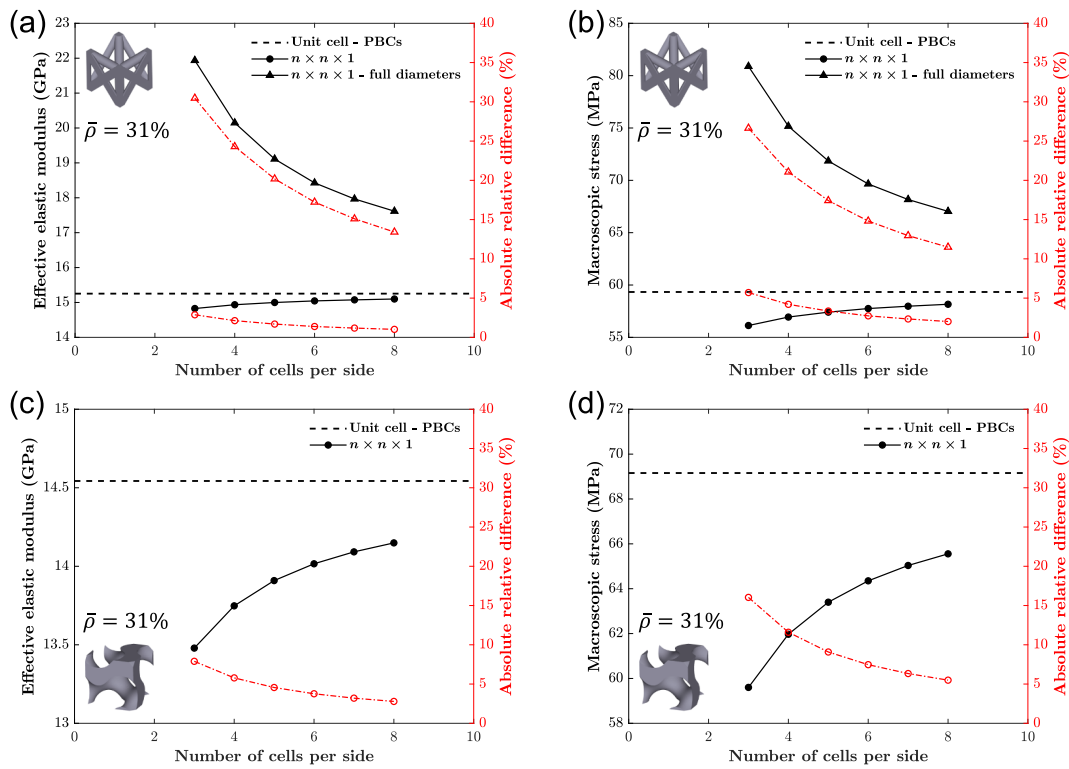
Fig.3. Influence of boundary effects on the effective elastic modulus and macroscopic stress at the maximum imposed strain for the (a-b) FBCCZ and (c-d) gyroid structures. The red open markers (circles, triangles) refer to the absolute relative difference between the response of the unit cell and the $n \times n \times 1$ structure. (For interpretation of the references to colour in this figure legend, the reader is referred to the web version of this article.)
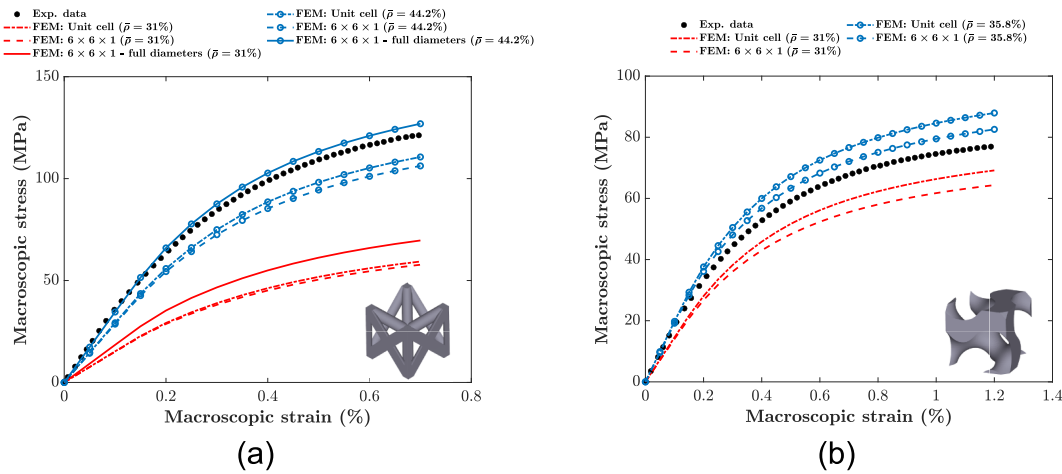

Fig.4. Comparison between experimental and simulated stress–strain response of (a) FBCCZ and (b) gyroid cellular materials considering different FE models and the as-designed and as-built relative densities.

3.2. Finite element model selection

3.2.1. Boundary effects

The various models described so far (unit cell with PBCs vs. $6 \times 6 \times 1$ layer structure) are compared to select which one reproduces the experimental data best. While using only one single cell with PBCs is less computationally demanding thanks to the reduced number of degrees of freedom of the FE model, it theoretically represents a cellular structure of infinite dimensions, and it can be a good approximation of actual structures with a minimum number of cells.

Fig. 3 (a-d) compares the stress–strain response of the FBCCZ and gyroid structures with a relative density of 31 % obtained by different

models: $n \times n \times 1$ structure with increasing numbers of cells per side, n, and the unit cell with PBCs. The response is evaluated in terms of the effective elastic modulus from linear elastic simulations and the macroscopic stress from non-linear elastoplastic simulations, both calculated at the highest macroscopic strain used in experiments (i.e. $\varepsilon_a = 0.7\%$ for the FBCCZ and $\varepsilon_a = 1.2\%$ for the gyroid). The macroscopic stress is the ratio of the applied axial force F to the cross-section area A_0 obtained by intersecting the volume occupied by the cellular structure envelope (unit cell or one-layer structure) with a transversal plane. In other words, the macroscopic stress is a nominal stress that considers the cellular structure a homogeneous material, not a porous structure. The macroscopic strain is the imposed displacement divided

by the length of the cell side. The $n \times n \times 1$ structures with and without full diameters at the boundary cells are presented for the FBCCZ in Fig. 3 (a-b). In fact, the additional stiffness added by the full diameters can be considered a boundary effect that vanishes with a high number of cells.

As can be seen, the macroscopic response of the $n \times n \times 1$ cellular structure with increasing the number of cells approaches the unit cell with PBCs from below. The PBCs models are then stiffer. This trend can be explained by considering that, unlike PBCs models, in $n \times n \times 1$ models, the cells at the boundaries freely deform at least over one lateral face, and, therefore, their response is less stiff than the interior cells, which are fully embedded.

A different behaviour characterises the model of FBCCZ cells with full diameters. In this model, the FBCCZ cells at the boundaries have full diameters and are then stiffer; hence, the macroscopic response of such $n \times n \times 1$ structure approaches the PBCs unit cell from above (see black triangles in Fig. 3 (a-b)). Nevertheless, in the case of both the $n \times n \times 1$ structure with and without full diameters, when the number of cells is high enough, the contribution of the cells at the boundaries becomes negligible compared to the interior cells, which, on the opposite, behave like the unit cell with PBCs. This is the reason why both models approach asymptotically the response of the PBCs unit cell model.

The absolute relative difference between the effective elastic modulus predicted by the unit cell and the $6 \times 6 \times 1$ structure is lower than 5 % for both cellular structures. This difference is slightly higher for the macroscopic stress at the maximum imposed strain amplitude but still below one-tenth, suggesting that the unit cell model can be considered satisfactory to simulate the response of cellular structures. However, the values of the effective elastic modulus and maximum macroscopic stress of the FBCCZ $6 \times 6 \times 1$ structure with full diameters are considerably above 10 % compared to the unit cell, thus questioning the use of the unit cell for the FBCCZ.

3.2.2. As-designed versus as-built relative density

The simulated stress–strain response with different FE models is compared against the experimental data in Fig. 4 (a-b). The applied macroscopic strain is equal to the maximum strain imposed in the cyclic tests. For the experiments, the macroscopic stress is defined in Section 3.2.1, where the cross-section area A_0 is the intersection of the volume occupied by the cellular specimen envelope with a transversal plane. It is evident that the mechanical response is underestimated for each model with the as-designed (evaluated using the nominal geometry) relative density of 31 %. The disagreement is evident when the stiffness predicted by the models is compared with that obtained from the experiments.

This difference comes from the geometrical deviations between the as-designed geometry and the as-built geometry manufactured by the AM process. In fact, the feature size of the cellular structures is close to the manufacturing limit of the AM machine; geometrical and dimensional deviations are inevitable. Such deviations, in turn, are responsible for the higher relative density of the as-built cellular structures compared to the as-designed ones.

Many studies emphasise the relevance of considering the as-built geometry in the simulation process [23,36,37,38,39]. The geometrical deviations are usually estimated using computed tomography (CT) when an accurate representation of the actual geometry is sought. However, CT analyses are only sometimes available due to the time-consuming procedure and expensive experimental apparatus. Therefore, the following procedure aims to determine the relative density of the as-built cellular structure through measurements of its mass; that is, a relative density that accounts for the dimensional and geometrical deviations of the additively manufactured structure from its theoretical geometry obtained by CAD. Several reasonable assumptions were considered:

- the volumetric mass density of the 316L steel, ρ_{316L}, is 8.00 kg/mm^3;

- the mass difference between the as-built and as-designed specimens is concentrated only in the cellular part, not in the grip sections, whose geometry can be manufactured with greater accuracy;
- the cellular part of the specimens consists of two portions: one with a constant relative density and the other with an increasing relative density towards the grip section. The mass increment in percentage is considered equal in both portions.

Based on those hypotheses and assuming that the external dimensions of the envelope of the cellular structure are the same between the as-built and as-designed specimens, the corrected relative density can be calculated.

The first step is measuring the mass of each specimen, m^{exp}, using a high-precision scale. The average values are 85.7506 g (standard deviation equal to 0.0482 g) for the FBCCZ and 76.346 g (standard deviation equal to 0.1569 g) for the gyroid.

The second step consists of evaluating the theoretical mass of the whole specimen, m^{CAD}, by multiplying the volume predicted by the CAD models and the volumetric mass density of the 316L steel; the values are 78.8505 g (for FBCCZ) and 73.7834 g (for gyroid), respectively. In the same step, the theoretical mass of different parts of the specimen is also calculated: m_{cell}^{CAD} – mass of the whole cellular part of the specimen – and $m_{cell,\bar{\rho}} = cost^{CAD}$ – mass of the cellular part considering only the portion with a constant relative density ($\bar{\rho} = cost$).

Then, the mass of the as-built cellular part with a constant relative density can be estimated:

$$m_{cell,\bar{\rho}} = cost^{exp} = \frac{(m^{exp} - m^{CAD})}{m_{cell}^{CAD}} m_{cell,\bar{\rho}} = cost^{CAD} + m_{cell,\bar{\rho}} = cost^{CAD} \quad (3)$$

where the second and third assumptions stated at the beginning of the procedure are exploited.

Once $m_{cell,\bar{\rho}} = cost^{exp}$ is known, the relative density of the as-built cellular specimen, within the constant relative density portion, can be estimated using the definition of relative density:

$$\bar{\rho}_{cell,\bar{\rho}} = cost^{exp} = \frac{\rho_{cell,\bar{\rho}} = cost}{\rho_{316L}} = \frac{m_{cell,\bar{\rho}} = cost^{exp}}{V_{cell,\bar{\rho}} = cost^{CAD}} \frac{1}{\rho_{316L}} \quad (4)$$

where $\rho_{cell,\bar{\rho}} = cost$ is the density of the cellular material calculated by dividing $m_{cell,\bar{\rho}=cost}^{exp}$ by the volume of the cellular part with constant relative density, including the hollow regions ($V_{cell,\bar{\rho}} = cost^{CAD}$).

This procedure returns the estimated relative density of the as-built FBCCZ and gyroid specimens as 44.2 % and 35.8 %, respectively, which differ from the nominal values by 43 % and 15 %. Similar values can be found in the literature for both strut- and TPMS-based cellular structures [40–43]. The gyroid structure then appears to be manufactured with a tighter tolerance. This outcome is not surprising, as other authors reported the high-quality printability of TPMS-based cellular materials compared to the strut-based ones [44].

Finally, the FBCCZ geometry used in the FE simulations was updated considering the relationship between the strut diameter and the relative density. In contrast, the relationship between the parameter t (constant parameter of the gyroid *iso*-surface equation) and the relative density was used for the gyroid cell. As shown in Fig. 4 (a-b), the recalibrated relative densities give acceptable results despite the simplified procedure assumptions. It must be noted that the proposed procedure considers the role of relative density without directly including geometrical deviations in the FE models, such as strut waviness and thickness variation.

Based on the presented results, the correction on the relative density will be adopted in the following analyses. Furthermore, the cyclic elastoplastic response of the FBCCZ specimens is modelled by the $6 \times 6 \times 1$ structure with full diameters despite being the most computationally demanding among the considered models. In fact, the $6 \times 6 \times 1$ structure with full diameters requires computational times forty times longer than the unit cell when the same loadings and boundary
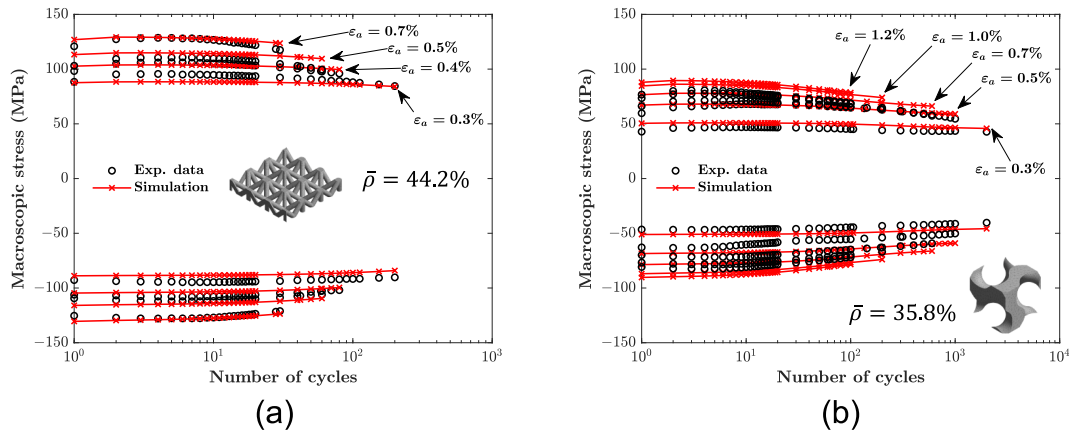
Fig.5. Experimental and simulated cyclic stress response: maximum and minimum macroscopic stress versus the number of cycles for the (a) FBCCZ and (c) gyroid structure.

Table 2
Mean absolute percentage error (MAPE) evaluated between the simulated and experimental macroscopic stress amplitudes throughout the test and absolute percentage error (APE) calculated for the first and half-life cycles.

	ε_a(%)	MAPE (%)	APE ($N = 1$)	APE ($N = N_f/2$)
FBCCZ	0.3	4.58	2.60	3.78
	0.4	1.07	1.44	0.62
	0.5	4.90	7.84	6.53
	0.7	1.70	4.56	3.29
Gyroid	0.3	10.04	13.64	10.26 (N=2000)
	0.5	9.89	10.64	15.24
	0.7	10.67	14.07	13.60
	1.0	11.25	14.18	12.50
	1.2	11.10	13.21	11.62

conditions are applied. Nevertheless, this choice led to a more accurate representation of the experimental mechanical response. The behaviour of the gyroid, on the other hand, was modelled by the unit cell with PBCs, leading to a reduced computational effort without losing excessive accuracy. Similarly to the computational times required by FBCCZ models, the gyroid unit cell is 36 times faster than the 6×6×1 structure.

Overall, Fig. 4 (a-b) demonstrates that the gyroid unit cell FE model with a 35.8 % relative density overpredicts the experimental macroscopic stresses by 10 to 15 %, whereas the 6×6×1 structure with full diameters and a 44.2 % relative density only slightly overestimates the response of the FBCCZ.

4. Cyclic elastoplastic response

4.1. Macroscopic cyclic stress–strain response

The macroscopic cyclic elastoplastic response of the cellular materials was simulated until the half-life cycle for all the strain amplitudes considered in the experiments. The FE models used in the simulations are the 6×6×1 FBCCZ structure with full diameters and the gyroid unit cell with the relative densities calibrated in Section 3.2.2.

The evolution of the simulated maximum and minimum stress for subsequent cycles at different strain amplitudes is compared with the experiments in Fig. 5 (a-b). The overall trend of the stress evolution during cycling is captured by the FE simulations for both cellular materials. As also suggested by the results in Section 3.2.2, the cyclic response simulated by the FBCCZ model is closer to the experimental values than the gyroid model, which overestimates the maxima and underestimates the minima of the stress. This difference in model accuracies, emphasised qualitatively in Fig. 5, is further highlighted by some quantitative metrics in Table 2, where the mean absolute percentage error (MAPE) [45] between the simulated and experimental stress amplitudes is reported for each test. The absolute percentage error (APE) at the first and half-life cycles is also given as a local indicator of the accuracy. The equations for APE and MAPE are reported in Appendix B. The MAPE is constantly below 5 % for the FBCCZ structure, with an average value of nearly 3 % among the strain amplitudes. On the contrary, the MAPE is almost always higher than 10 % for the gyroid structure modelled by the unit cell with PBCs, with an average value of 10.6 %.
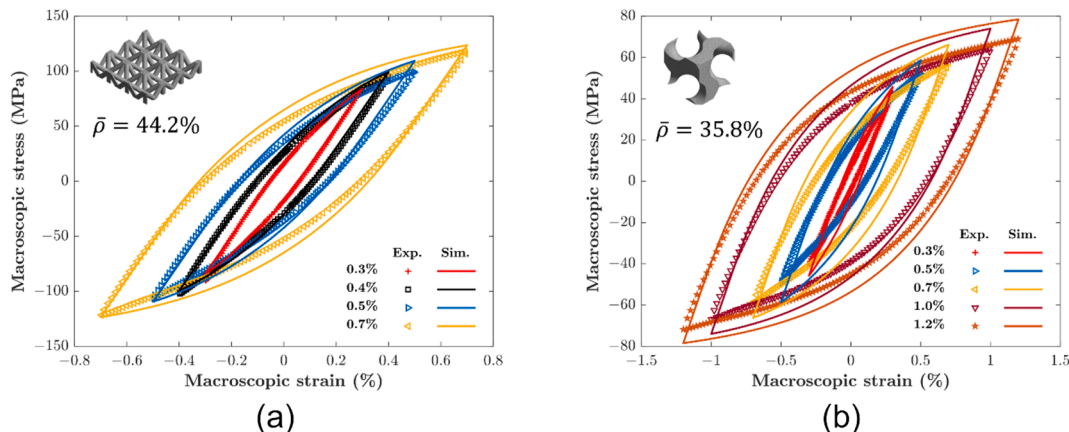

Fig.6. Experimental and simulated half-life macroscopic stress–strain hysteresis loops for the (a) FBCCZ and (b) gyroid structure.
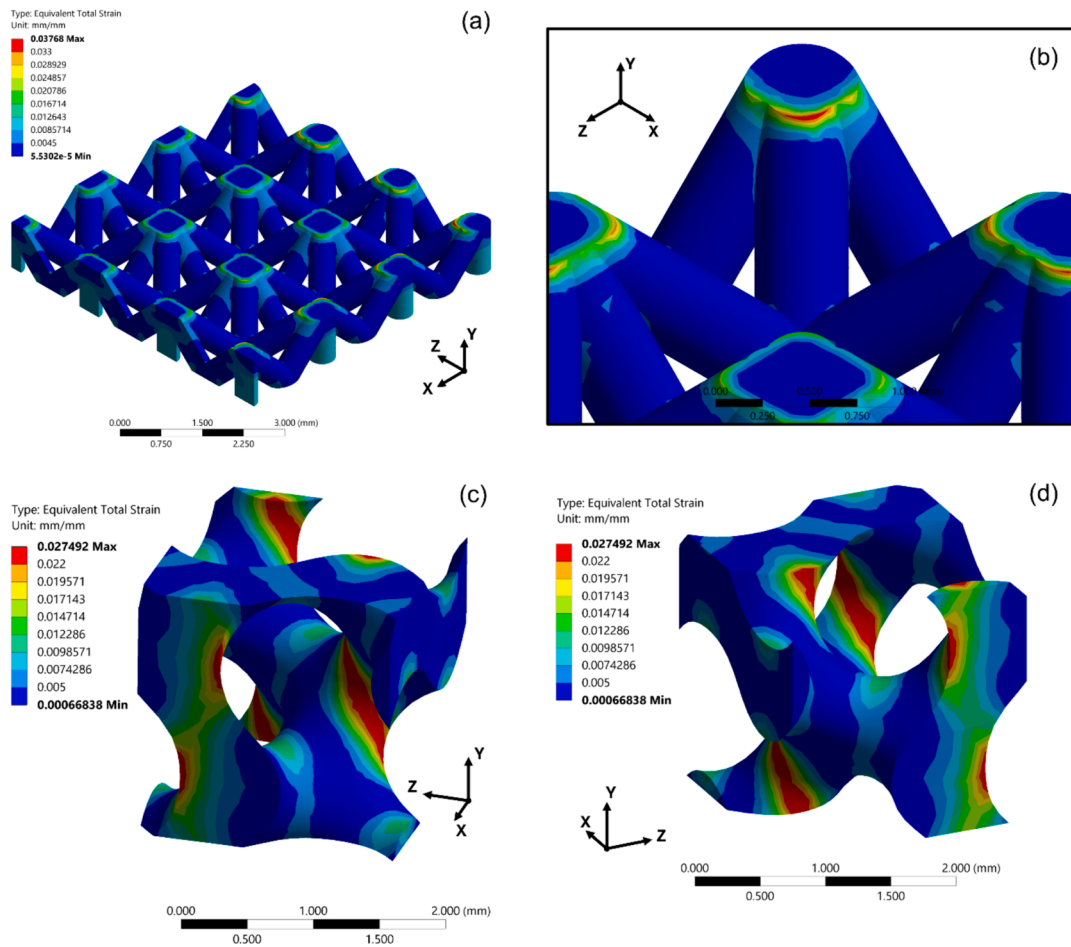
Fig.7. Equivalent total strain field: (a) 6×6×1 FBCCZ structure with full diameters loaded at 0.7 % strain amplitude where (b) is a close-up on the critical point; (c) and (d) gyroid unit cell loaded at 1.2 % strain amplitude.

A comparison of the simulated and experimental macroscopic stress–strain hysteresis loops at half-life is shown in Fig. 6 (a-b). The figure confirms, once again, that the FBCCZ model has a better prediction accuracy than the gyroid model, which has instead the tendency to estimate larger stress values. The accuracy achieved by the simulated hysteresis loops at different cycles is comparable to the half-life ones in Fig. 6 (a-b).

It is worth noticing that the material properties obtained from bulk cylindrical specimens are suitable to model the response of struts and nodes with a significantly lower size. In fact, once the relative density has been corrected, the linear and non-linear portions of the macroscopic stress–strain behaviour of the cellular structures are well reproduced by the FE simulations. On the other hand, several studies propose to adopt the mechanical properties obtained from testing small-size specimens or micro-struts [46,47]. However, as pointed out in similar studies, the different mechanical properties obtained from micro-struts compared to the standard-size specimens are mainly related to the difficulty in defining the load-bearing area and, hence, the stress [48,49]. Other effects associated with the different microstructure of micro-struts compared to the standard-size specimens are likely to have minor influences. Alternatively, Magarò et al. performed nano-indentations to characterise the local elastoplastic behaviour in the struts and nodes [50]. This approach appears effective in capturing the microstructure influence on the mechanical behaviour of small geometrical features. However, characterising the cyclic elastoplastic response requires performing cyclic indentation tests and developing empirical correlations between the test results and the constitutive model. Ultimately, it seems reasonable to adopt the mechanical properties of standard-size specimens in the constitutive model for the FE simulations and, as a separate correction, to modify the geometry of the as-designed cellular structure. This choice avoids sensitive and challenging strain-controlled cyclic tests in the elastoplastic regime using micro-struts.

4.2. Microscopic stress/strain fields

The way stress and strain are distributed within cellular structures differs greatly between FBCCZ and gyroid topologies when subjected to macroscopic uniaxial loading. To highlight the critical point of each cellular material, the equivalent total strain field is reported in Fig. 7 for the FE models of the 6×6×1 FBCCZ structure with full diameters and the gyroid unit cell. The equivalent von Mises stress may not be suitable for identifying the critical region because the values tend to saturate and redistribute due to the non-linear material response.

The results presented in Fig. 7 correspond to the maximum point of the second cycle, where the FBCCZ was cyclically loaded at 0.7 % strain amplitude and the gyroid at 1.2 % strain amplitude. The vertical struts of the FBCCZ structure bear most of the load and experience a high strain level, as highlighted in Fig. 7 (a). Nevertheless, the strain further rises towards the sharp notches located at the junctions of the struts. Here, the local strain value predicted by the FE method increases with the decrease in mesh size due to the geometric singularity. Among the different junctions, the nodes cut by the upper face of the model present the highest strain values. In particular, the highest strain value is positioned at the corner edge of the structure and depicted in the close-up of Fig. 7 (b). On the other hand, the strain is more evenly distributed within the gyroid unit cell, as can be appreciated in Fig. 7 (c-d). Due to the
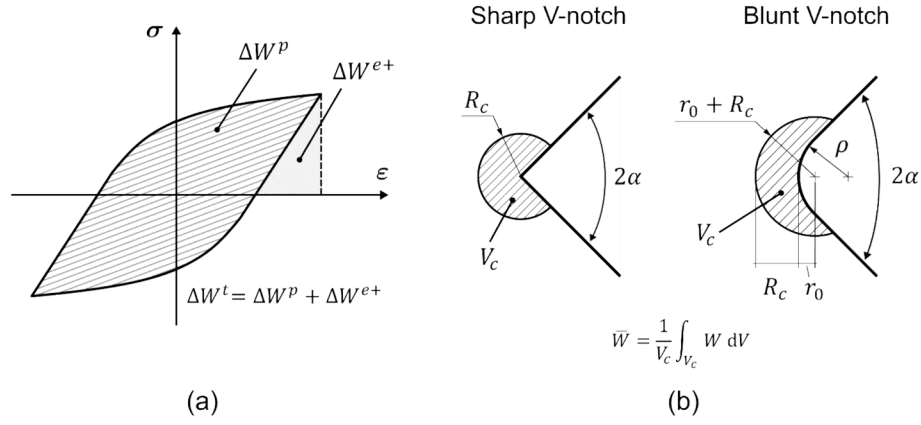
Fig.8. (a) Positive elastic, plastic and total strain energy density in a stress–strain cycle under uniaxial loading condition. (b) Control radius and volume (area) for bi-dimensional sharp and blunt V-notches.

unique geometry of the gyroid, several points attain the same maximum strain level and are thus critical. In fact, the most strained zone envelops the geometry following a helical path around the pseudo-struts (see the red region in Fig. 7 (c-d)). Additionally, the absence of sharp notches in the geometry leads to a mild strain gradient toward the critical region.

5. Fatigue life assessment

5.1. Theory of strain energy density method

5.1.1. Ellyin's energy-based approach

The fatigue damage parameter considered in this work is the strain energy density (SED), which can account for the influence of both the stress and strain. The SED is a scalar quantity that intrinsically encompasses the multiaxial stress/strain state and can include the contribution of plastic deformation, covering both the HCF and LCF regimes. Furthermore, fatigue assessments based on SED are straightforward compared to critical plane-based methods that require a time-consuming post-processing phase. However, the SED cannot estimate the plane where the crack is likely to nucleate and propagate. Finally, a promising method, which will be discussed in the next Section 5.1.2, to account for the notch effect in fatigue involves using the SED averaged in a volume.

The criterion proposed by Golos and Ellyin [51] defines a link between the total SED and the number of reversals to failure, $2N_f$:

$$\Delta W^t = \Delta W^p + \Delta W^{e+} = \kappa_t \left(2N_f\right)^{\alpha_t} + \Delta W_0^t \tag{5}$$

where ΔW^p is the plastic SED in a cycle and ΔW^{e+} is the elastic SED of the positive cycle portion. These quantities are depicted in Fig. 8 (a) for the uniaxial loading case. The material constant ΔW_0^t is equal to the tensile elastic SED at the fatigue endurance limit, whereas the constants κ_t and α_t rule the finite life fatigue curve.

As noted in Eq. (5), the energy-based approach can account for elastoplastic deformation. Furthermore, for a generic stress/strain multiaxial state, the plastic SED per cycle is:

$$\Delta W^p = \int_{cycle} \sigma_{ij} d\varepsilon_{ij}^p \tag{6}$$

where σ_{ij} and ε_{ij}^p are the components of the stress and plastic strain tensor with the indices $i, j = 1, 2, 3$. The product inside the integral is between components with the same indices and is intended as the sum over of the nine components. Given the hypothesis of incompressibility under plastic deformation, the plastic SED is strictly deviatoric.

On the other hand, the positive elastic SED also accounts for the hydrostatic deformation and can be calculated as follows [52,53]:

$$\Delta W^{e+} = \frac{1}{2E}\left[\left(I_1^{max}\right)^2 - \left(I_1^{min}\right)^2\right] - \frac{1+\nu}{E}\left[I_2^{max} - I_2^{min}\right] \tag{7}$$

where

$$I_1^{max} = \sigma_1^{max} H(\sigma_1^{max}) + \sigma_2^{max} H(\sigma_2^{max}) + \sigma_3^{max} H(\sigma_3^{max}) \tag{8}$$

and

$$
\begin{aligned}
I_2^{max} = &\sigma_1^{max}\sigma_2^{max}H(\sigma_1^{max})H(\sigma_2^{max}) + \sigma_2^{max}\sigma_3^{max}H(\sigma_2^{max})H(\sigma_3^{max}) \\
&+ \sigma_3^{max}\sigma_1^{max}H(\sigma_3^{max})H(\sigma_1^{max})
\end{aligned}
\tag{9}
$$

in which H is the Heaviside function and σ_1, σ_2 and σ_3 are the principal stresses. Analogous expressions are defined for I_1^{min} and I_2^{min}.

5.1.2. Extension of the average strain energy density method

In the presence of notches, Ellyin's criterion must be expanded to include the notch sensitivity. One natural way is to adopt the average SED method proposed by Lazzarin and Zambardi [54] for predicting static and HCF failures of components with sharp V-shaped notches. This method was initially formulated for material with a linear elastic behaviour but then was extended to include generalised plasticity [55,56]. For example, Torabi et al. tried to predict the static failure of notched specimens made of ductile material using the equivalent material concept [57]. Nonetheless, to the best of the author's knowledge, the average SED method was never applied to assess the strain-controlled LCF data of notched specimens. Therefore, the present study constitutes a first attempt.

The SED approach originally formulated for static failure states that a component with a V-notch fails when the average SED calculated in a control volume centred around the notch equals a critical value of the material:

$$\overline{W}(V_c) = \frac{1}{V_c}\int_{V_c} W dV = W_c \tag{10}$$

where V_c is the control volume, which is a material property to be calibrated from the experiments, and the overbar indicates the average operation over the volume. The critical value W_c is also a material property and corresponds to the SED value at static failure for plain specimens.

With fatigue loadings, the average SED method can be written by using the range values for evaluating the event of fatigue failure:

$$\overline{\Delta W}(V_c) = \Delta W_c \tag{11}$$

where V_c is usually different from the case of the static failure and it depends on the number of cycles to failure. The critical value ΔW_c is the
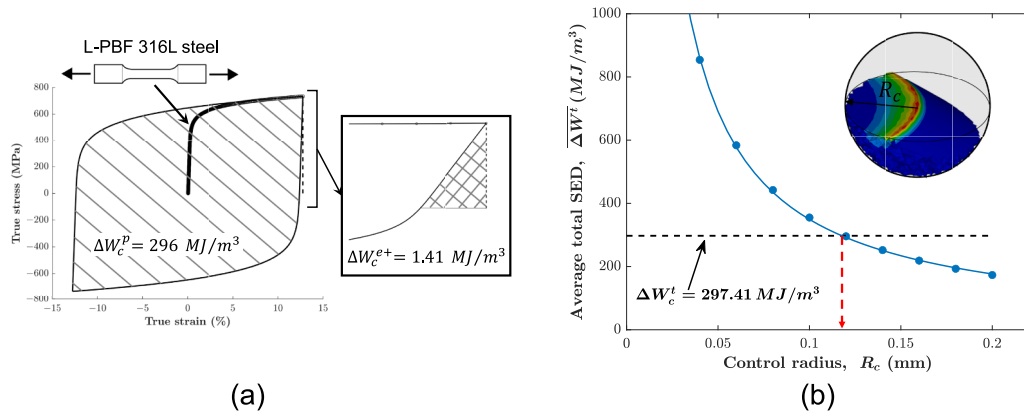
Fig.9. Calibration of the control radius size: (a) plastic and positive elastic SED evaluated on the tensile test curve magnified by a factor of 2; (b) average total SED numerically evaluated for different control radius (light blue circles) and critical total SED for the bulk material (black dashed line). (For interpretation of the references to colour in this figure legend, the reader is referred to the web version of this article.)
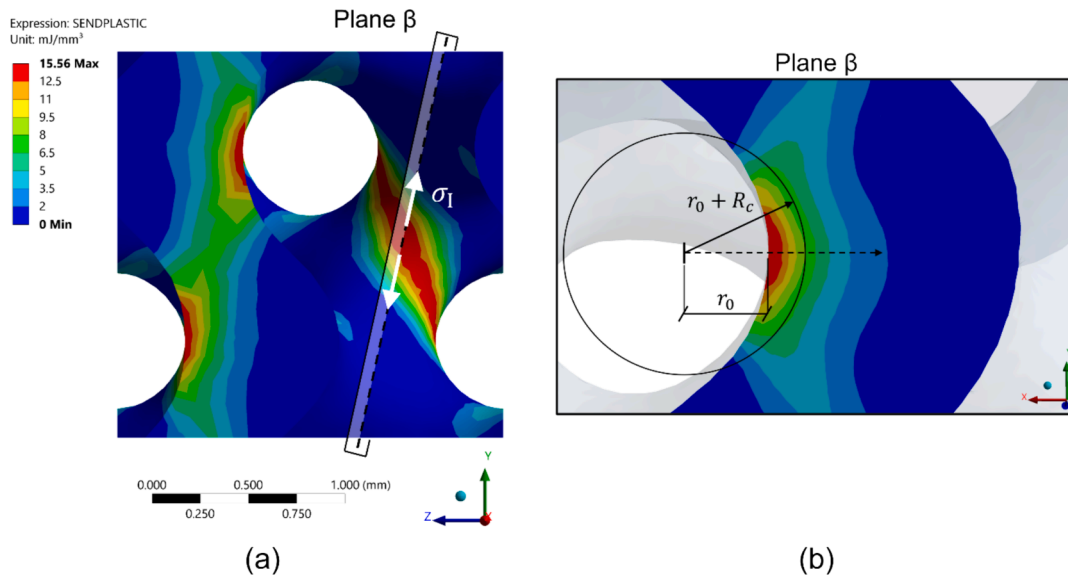

Fig.10. Plastic SED contour plots and definition of the control volume. (a) Section plane β aligned with the maximum stress principal direction. (b) Distribution over the plane β and control volume outline.

SED range associated with the fatigue failure at a given number of cycles to failure.

The approach proposed in this work expands Ellyin's criterion of Eq. (5) to include the notch effect by using the average SED method of Eq. (11):

$$\overline{\Delta W^t}(V_c) = \kappa_t \left(2N_f\right)^{\alpha_t} + \Delta W_0^t$$

$$\overline{\Delta W^t}(V_c) = \overline{\Delta W^p}(V_c) + \overline{\Delta W^{e+}}(V_c) \qquad (12)$$

where $\overline{\Delta W^p}(V_c)$ and $\overline{\Delta W^{e+}}(V_c)$ are the plastic SED and positive elastic SED averaged in the control volume V_c. The sum of these two contributions gives the average total SED, $\overline{\Delta W^t}(V_c)$. The tensile elastic SED at the fatigue limit ΔW_0^t will be neglected in the following analyses. Therefore, the parameter κ_t now incorporates the parameter ΔW_0^t, and, for $2N_f$ tending to infinity, the model does not include an endurance limit. This assumption is acceptable as long as the studied regime is far from the HCF regime.

As a final aspect, the average SED method was developed for notches that can be studied as bi-dimensional. To obtain the control volume, a circle of radius R_c, whose centre is coincident with the notch tip, is usually intersected with the material surrounding the notch. For sharp V-notch, the resulting control volume (area) is outlined in Fig. 8 (b). The average SED approach was also extended to predict the failures of components weakened by blunt V-notches with a curvature radius, ρ [58]. This specific case is shown in Fig. 8 (b), where the control volume can be obtained by shifting the circular sector by a quantity r_0 from the notch tip and changing the radius to $(r_0 + R_c)$. The parameter r_0 depends on the curvature radius and the notch angle, 2α. When the notch is instead three-dimensional, the control volume is sometimes simplified as the intersection between a sphere with radius R_c surrounding the critical point and the material around the notch [23]. In conclusion, the calibration of the control volume consists of identifying the control radius R_c by comparing the fatigue results of notched and plain specimens, irrespectively to the notch geometry.

5.2. Calibration of the control volume shape and size

The geometry of the control volume is determined by using a sphere centred at the critical point of the cellular structure as the intersecting
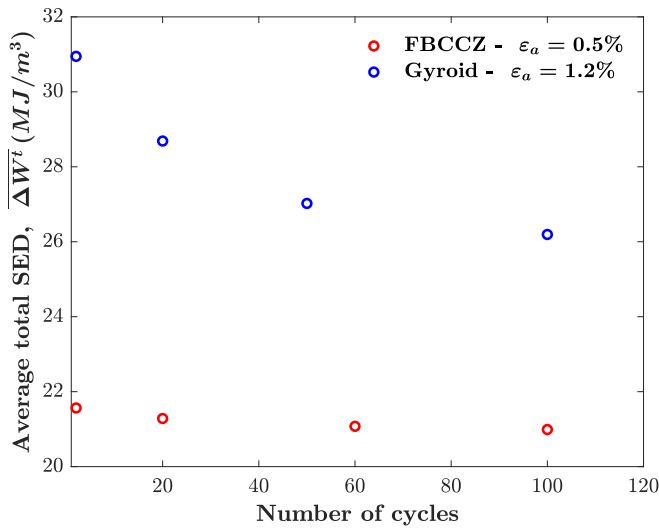
Fig.11. Numerical values of the average total SED versus number of cycles for the FE simulations of the FBCCZ and gyroid structure cyclically loaded at 0.5% and 1.2% strain amplitude, respectively.

Table 3
Experimental and estimated number of cycles to failure for the FBCCZ and gyroid cellular materials.

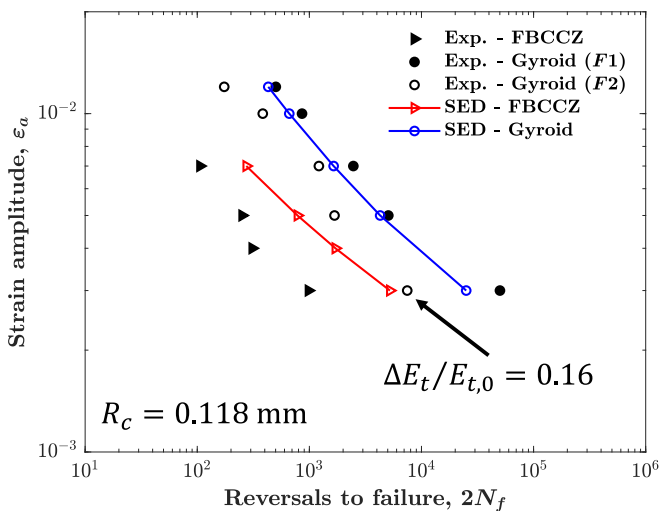|	ε_a(%)	$\overline{\Delta W^t}$(MJ/m^3)	N_f(cycles)	
		Simulations	Experiments	Simulations
FBCCZ	0.3	6.896	492	2616
	0.4	13.51	155	854
	0.5	21.58	126	392
	0.7	40.59	53	137
Gyroid	0.3	2.689	25,057	12,533
	0.5	7.779	2531	2141
	0.7	13.82	1234	823
	1.0	23.88	430	331
	1.2	30.92	251	215

Fig.12. Comparison between experimental and estimated reversals to failure using the average total SED method in a strain-life plot for the FBCCZ and gyroid structures. Experimental data for the gyroid are reported based on two failure criteria: *F1* – 10% drop of the maximum stress compared to the linear softening; *F2* – 16% drop in the effective tensile elastic modulus (E_t) to the initial value.

object. The radius of the sphere is the control radius R_c, and its size is considered a material parameter. In the absence of fatigue data for notched and plain specimens, Molavitabrizi et al. proposed to estimate the critical distance by comparing the static failure of the cellular structures and plain specimens [25]. The choice was justified by considering that the static failure is nothing but a limiting case of an LCF failure with a fatigue life of only one cycle. A similar approach was followed in this work, where a comparison of the static behaviour between the FBCCZ and plain specimens enables the control radius R_c to be found. Nevertheless, it should be stressed that the natural way to calibrate R_c is to compare fatigue data of notched and plain specimens tested in the regime of interest (i.e. LCF); in theory, the value of R_c should change with the number of cycles to failure. In particular, the size should decrease with increasing the number of cycles to failure [59].

Considering that the control radius is assumed to be a material property independent of the notch geometry [60], the value of R_c calibrated for the FBCCZ is used to estimate the fatigue life of the gyroid structure. Nonetheless, the geometry of the gyroid has no sharp notches and the stress/strain raisers are located at blunt notches. Therefore, a different shape of the control volume is defined based on the theory discussed in Section 5.1.2.

5.2.1. FBCCZ cellular material

The procedure adopted to estimate the value of R_c is schematised in Fig. 9 (a-b). The energy on a complete cycle is computed so that Eq. (12) for fatigue loading can be applied with the control radius estimated under static loading. Firstly, the critical total SED for the bulk L-PBF 316L steel under static loading is evaluated. To this end, the monotonic true stress-strain curve of the material until the peak stress was considered. The monotonic curve was then mirrored twice to define a closed hysteresis loop, which was used – in place of the monotonic curve – to determine the total SED in Eq. (12) as the sum of the elastic and plastic strain energy densities, see Fig. 9 (a). The obtained total SED value is $\Delta W_c^t = 297.41$ MJ/m^3; it represents a property of the bulk material. For convenience, it is reported in Fig. 9 (b) as a horizontal dashed line for subsequent analyses.

Once the critical total SED is known, the second step is to determine the control volume V_c of the FBCCZ cell, to be used in Eq. (12) as well. For this purpose, the response of the 6×6×1 FBCCZ structure subjected to a strain-controlled cycle was simulated by the FE model. The maximum strain amplitude in the strain-controlled cycle, namely 3.56 %, corresponds to the strain measured at the peak force during the experimental tensile test of the FBCCZ specimen. In simulations, the strain amplitude was applied for one-quarter cycle and then one cycle in order to simulate one closed loop. For this simulation, the material model is elastoplastic with a multilinear kinematic hardening, and it is calibrated on the same monotonic true stress-strain curve of the L-PBF 316L steel mentioned above. Based on the simulated response of the 6×6×1 FBCCZ structure, the total SED $\overline{\Delta W^t}(V_c)$ averaged over a spherical control volume, centred at the critical point, was evaluated for different control radii. An example of control volume considered in this step is illustrated in the inset of Fig. 9 (b). Although the average SED method is less mesh sensitive [61], the FE mesh was refined around the critical point because the volume-free procedure was applied to evaluate the average SED [62]. In fact, the shape of the control volume is approximated by tetrahedrons in the volume-free approach leading to less accurate calculations, despite being more straightforward to implement. Consequently, it was decided to decrease the element size in a sphere with a radius slightly higher than the expected R_c.

The trend of the average total SED for different control radii is depicted in Fig. 9 (b) as markers. The continuous curve interpolates the numerical values using a power law function; its intersection with the critical SED (dashed line) yields an estimate of the control radius $R_c = 0.118$ mm, which can be thought as a material property. This value will be used to assess the fatigue life of the FBCCZ structure.
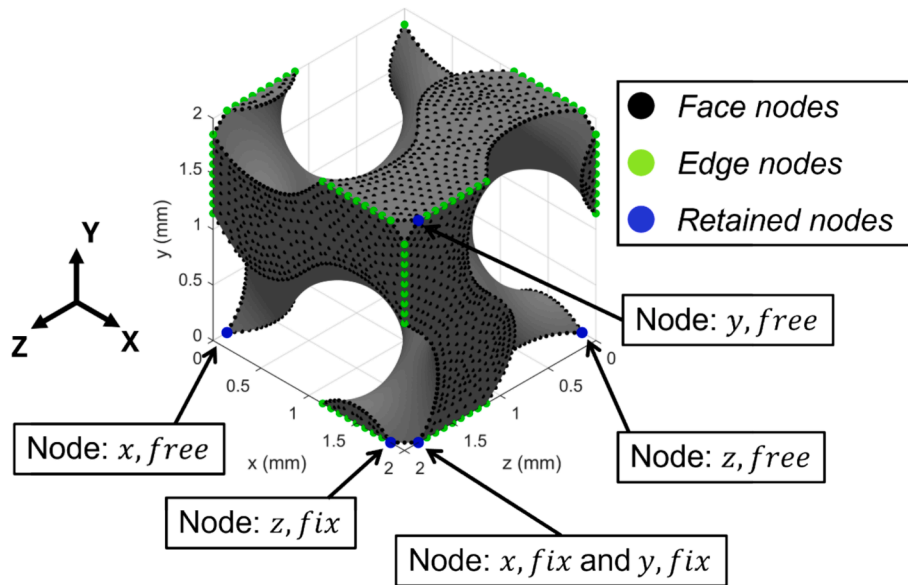
Fig.13. Mesh nodes of the gyroid unit cell FE model used to implement the periodic boundary conditions. Black and green solid circles are the *face* and *edge nodes*, respectively, whereas the *retained nodes* are indicated with blue solid circles. (For interpretation of the references to colour in this figure legend, the reader is referred to the web version of this article.)

5.2.2. Gyroid cellular material

The control radius estimated for the FBCCZ structure is also used for the gyroid. However, a change in the control volume shape is necessary to account for the case of blunt notches [59,63]. As discussed in Section 4.2, several points attain the same maximum stress/strain level within the gyroid cell. For that reason, one point that allows defining the entire control volume was selected from that region to be the critical point. Fig. 10 (a) shows the plastic SED contour of the gyroid and the selected critical point. In addition, a plane β, passing through the vector normal to the point and the vector defining the maximum principal stress direction is shown schematically. Eventually, the plastic SED contour was analysed on a section obtained by using the plane β, and a control volume with a radius of $(r_0 + R_c)$ and centred at a distance r_0 from the critical point was defined, see Fig. 10 (b). The value of r_0 was set equal to half of the curvature radius calculated in the critical point, with the radius lying in the plane β. The vector normal to the critical point and the curvature radius can be calculated analytically using the equation of the gyroid surface [31]. Finally, a mesh refinement was created around the critical point to obtain accurate values of the average total SED for the fatigue life assessment.

5.3. Low cycle fatigue curves

The average SED criterion described in Section 5.1.2, i.e. Eq. (12), was used to estimate the fatigue life of the FBCCZ and gyroid structures, together with the control volume shape and size calibrated in the previous Section 5.2. Cyclic FE simulations were carried out on the 6×6×1 FBCCZ structure with full diameters and the gyroid unit cell by imposing the same strain amplitudes used in experiments.

In the case of LCF loading conditions, the average total SED changes during cycling due to the cyclic hardening/softening of the material. Only when the material reaches a stabilised condition can a unique value of the average total SED be obtained and adopted in the fatigue criterion of Eq. (12).

To comprehend the cyclic evolution of the average total SED, two FE simulations were performed. A cyclic load was applied to the FBCCZ and gyroid structures for 100 cycles. The former loaded at 0.5 % strain amplitude, the latter at 1.2 %. This value of 100 cycles aligns with the half-life of the gyroid specimen tested at 1.2 %. The same value was selected for the simulation of the FBCCZ tested at 0.5 % for a straightforward comparison, despite the half-life being at 60 cycles. These preliminary simulations show that the average total SED decreases with increasing the number of cycles, as depicted in Fig. 11. While for the FBCCZ structure, the decrease can be considered negligible, for the gyroid, the average total SED evaluated in the control volume drops by 16 % from the initial value. Furthermore, an apparent stabilisation of the average total SED has yet to be achieved. Therefore, due to the high computational effort of simulating thousands of cycles until reaching a stabilised value of the average total SED, the latter was evaluated at the second cycle for all the strain amplitudes, thus providing more conservative results and reducing the simulation time.

The average total SED evaluated at the second cycle was used in Eq. (12) to obtain the number of cycles to failure. Both quantities are reported in Table 3. The material parameters in the LCF model defined by Eq. (12) are equal to $\kappa_t = 1184.84\,\text{MJ/m}^3$ and $\alpha_t = -0.6010$, where ΔW_0^t was neglected, as mentioned in Section 5.1. The experimental numbers of cycles to failure are also reported in Table 3, while the strain-life curves are depicted in Fig. 12.

The estimated cycles to failure listed in Table 3 are close to the experimental values for the gyroid, which it can also be appreciated by the data in Fig. 12. The only exception is the test at 0.3 % strain amplitude, where the estimated cycles to failure are nearly half the experimental value. On the other hand, the estimated fatigue lives for the FBCCZ are always two to more times higher than the experimental data and the predicted strain-life curve is placed on the right to the experimental values, thus providing non-conservative results within the tested strain amplitude interval. This latter outcome can be ascribed to the fact that the control radius was estimated from the material static response. The influence of the sharp notch is expected to be lesser under static loading than fatigue loading. Therefore, the control radius estimated from the static material behaviour is larger than the radius estimated from fatigue loading. In turn, a larger control radius leads to lower average total SEDs and, hence, higher numbers of cycles to failure. In summary, the control radius estimated from the static material properties may explain the non-conservative estimates observed for fatigue loadings.

The results obtained for the gyroid are instead less straightforward to be explained. A degree of non-conservatism similar to the case of the FCBBZ was expected, considering that the control radius used in the fatigue assessment is the same. Even though the average total SED at the

half-life cycle is used, the degree of non-conservatism remains less pronounced than in the case of the FBCCZ structure. A possible explanation is related to the definition of the cycles to failure obtained from the experimental results. In Pelegatti et al. [29], the failure criterion (*F1*) to define the number of cycles to failure was based on a 10 % reduction from the linear cyclic softening experienced by the maximum stress. Although the adopted criterion was the same for the FBCCZ and gyroid structures, an alternative failure criterion can be defined based on the drop in the tensile elastic modulus E_t (i.e. the effective elastic modulus estimated from the unloading portion of the cycle). This quantity might be more appropriate to define a damaged condition of the cellular structure than the decrease in maximum stress, which can also be related to the material softening.

When the cellular structures reached N_f cycles based on the *F1* criterion, the tensile elastic modulus declined by around 16 % for all the FBCCZ specimens, whereas a drop of 40 % was estimated for the gyroid specimens. This difference seems to suggest that a larger portion of the material in the gyroid structure than in the FBBCZ was damaged when a 10 % drop in the maximum stress was reached, thus questioning the consistency of the comparison. Therefore, if a new failure criterion (*F2*) is defined based on a 16 % drop of the tensile elastic modulus for both cellular materials, the fatigue lives of the gyroid specimens are lowered, as shown in Fig. 12 by the black open circles. The estimated cycles to failure using the average SED method are now non-conservative for both the FBCCZ and gyroid structures, which appears to be a more reasonable result. If a smaller control radius is selected for the LCF assessment, the average SED method is now expected to give accurate results for both cellular materials.

The above discussion emphasises that the comparison between estimated and experimental fatigue lives depends upon the failure criterion of cellular structures. Moreover, the control volume size calibration strongly influences the estimated fatigue lives using the SED approach.

As a final remark, the proposed procedure considers the influence of process-induced defects on fatigue life. In fact, the fatigue curve of the base material was obtained on bulk specimens, which were characterised by the presence of gas pores and lack-of-fusion defects. On the contrary, the effect of the surface roughness is not included, as it requires using a fatigue curve estimated by bulk specimens with as-built surface. However, the influence of the surface roughness in the LCF regime was found to be minor by several studies [14,64].

6. Conclusion

A methodology to assess the LCF lifetime of cellular materials is proposed and validated against experimental data obtained in a previous study. FE simulations were performed to reproduce the cyclic elasto-plastic response at the macro-scale, whereas the average total SED in a control volume at the micro-scale was adopted to estimate the cycles to failure of the cellular materials. The following outcomes on the applied methodology can be drawn:

- The FE model of a unit cell with PBCs can accurately replicate the macroscopic cyclic elastoplastic response of cellular structures characterised by layers of 6×6×1 cells along the loading direction. However, the struts with full diameters at the boundaries of the FBCCZ cellular specimen introduce a further effect that must be included in the simulations to achieve acceptable results.
- The macroscopic stress–strain response simulated by the as-designed geometries of the cellular structures largely underestimates the experimental response. An approximated procedure based on the mass measurement of the cellular specimens is adopted with satisfying performance to match the relative density of the as-built

cellular structure and recalibrate the geometrical dimensions of the FE model.
- The macroscopic cyclic elastoplastic response is well reproduced by the 6×6×1 FBCCZ structure, with absolute percentage errors calculated on the macroscopic stress amplitudes below 10 %. On the other hand, the macroscopic stress amplitudes predicted by the gyroid unit cell are over 10 % of the experimental values. Overall, the non-linear stress–strain response of the cellular materials is well-captured by using a constitutive material model calibrated on bulk cylindrical specimens with a considerably larger size than the features of the cellular structures.
- The average total SED method, in combination with a control volume size calibrated from the static properties of the L-PBF 316L steel and the FBCCZ structure, provides non-conservative fatigue lives for the FBCCZ. However, the estimated cycles to failure are close to the experimental values for the gyroid, suggesting that the higher fatigue lives of the gyroid specimens compared to the FBCCZ are likely due to a different fatigue failure process in the structure, which cannot be entirely captured by the simplified model adopted in this work.

Overall, the proposed methodology was proven to give acceptable results, especially when dealing with structures showing blunt geometrical features. Further improvements should be introduced to account for the as-built geometry of the cellular structures and especially to calibrate the control volume size when the actual geometry significantly differs from that nominally modelled. Furthermore, an in-depth understanding of the progressive damage of the cellular structures during the LCF loading can provide helpful insights to develop more physically consistent models. Nevertheless, the proposed methodology is yet an efficient, flexible and relatively inexpensive engineering tool.

CRediT authorship contribution statement

Marco Pelegatti: Writing – original draft, Methodology, Investigation, Formal analysis, Conceptualization. **Denis Benasciutti:** Writing – review & editing, Supervision. **Francesco De Bona:** Writing – review & editing, Supervision, Resources, Conceptualization. **Enrico Salvati:** Writing – review & editing, Validation, Supervision, Funding acquisition.

Declaration of competing interest

The authors declare that they have no known competing financial interests or personal relationships that could have appeared to influence the work reported in this paper.

Data availability

Data will be made available on request.

Acknowledgements

Appendix A. : Periodic boundary conditions

Owing to the lack of geometric symmetries of the gyroid, the faces of the cell warp when deforming. Therefore, approximating the PBCs by imposing the faces to remain flat during the deformation, as done for the FBCCZ cell, is inaccurate. In the case of the gyroid cell, the full equations that describe the PBCs must be imposed on the FE model as constraint equations.

A cell inside a cubic domain of side length l_0 can be taken as an example to explain the PBCs. A cartesian frame of reference Oxyz is positioned with its origin O at one of the cube vertices and its axes aligned with the cube edges. The PBCs equations constrain the homologous points of opposite faces to have the same displacement values minus the macroscopic strains along x, y and z:

$$\begin{cases} (u_{x+} - u_{x-}) = \overline{\varepsilon_x} l_0 \\ (v_{x+} - v_{x-}) = 0 \\ (w_{x+} - w_{x-}) = 0 \end{cases} \quad \begin{cases} (u_{y+} - u_{y-}) = 0 \\ (v_{y+} - v_{y-}) = \overline{\varepsilon_y} l_0 \\ (w_{y+} - w_{y-}) = 0 \end{cases} \quad \begin{cases} (u_{z+} - u_{z-}) = 0 \\ (v_{z+} - v_{z-}) = 0 \\ (w_{z+} - w_{z-}) = \overline{\varepsilon_z} l_0 \end{cases} \tag{13}$$

where u, v and w are the displacements along x,y and z, respectively. Subscript $x+$ indicates the points lying on the face with the maximum x coordinate ($x = l_0$), whereas the subscript $x-$ indicates the points at the minimum x coordinate ($x = 0$). The same notation, in which x is replaced by y and z, is used to indicate the points lying on the other four faces, that is, $y+$ and $y-$, and $z+$ and $z-$ to indicate the opposite faces along y and z, respectively. The macroscopic strains $\overline{\varepsilon_x}$, $\overline{\varepsilon_y}$ and $\overline{\varepsilon_z}$ define the average elongation/contraction of the cube along x,y and z.

In other words, the homologous points of opposite faces move by the same value along the direction perpendicular to the faces minus the elongation/contraction defined by the macroscopic strain. The latter can be imposed as an external load or caused by the lateral contraction/elongation of the cell.

The first requirement to implement the PBCs in the FE method is to define a periodic mesh on the FE model. A periodic mesh is characterised by having the same FE discretisation on the opposite faces of the unit cell, i.e. the number of nodes on the opposite faces is equal, and the location of the nodes in the planes of the faces is the same. Therefore, each node on one face has its counterpart on the opposite face to form a pair of nodes, which can then be coupled using constraint equations. The second step consists of forcing the Eqs. (13) on the nodes of the cube faces. However, the nodes on the edges (*edge nodes*) and vertices (*vertices nodes*) of the cubic domain are shared by more than one face, and over-constraints on these nodes must be avoided. Therefore, different sets of constraint equations are defined for the *edge* and *vertices nodes*, whereas Eqs. (13) are imposed on the nodes of the cube faces (*face nodes*), excluding the *edge* and *vertices nodes*.

The procedure to implement the PBCs is analogous to the one in the works of Omairey et al. [65] and Okereke et al. [32], where only slight changes are operated. As reported by Okereke et al., Eqs. (13) can be numerically implemented in the FE method by defining the slave nodes and the *retained nodes*. The *retained nodes* are four of the eight nodes at the vertices of the unit cell, where the load is prescribed. Meanwhile, the slave nodes are the remaining nodes on the six faces and twelve edges of the cubic domain, which are kinematically tied with the displacements of the *retained nodes*.

At this point, the specific case of the gyroid unit cell is considered. The same cartesian reference frame described for Eqs. (13) will be used, as well as the same notations for the different sets of *face nodes*. It is worth pointing out that now the concept of point is replaced with the concept of node, consistently with the FE method. The *edge nodes* are denoted by combining the previous notation; for example, $x+/y+$ denotes the nodes at the edges with coordinates $x = 1$ and $y = 1$. Finally, in the present work, five nodes on five of the cube edges are defined as *retained nodes* because solid material is not present in the vertices of the cubic domain, see Fig. 13. For the same reason, the *vertices nodes* are not present. The *retained nodes* are indicated with the subscripts x,*free*, y,*free*, z,*free*, x,*fix*/y,*fix* and z,*fix*.

The imposed PBCs constraint equations are reported and discussed in the following for each set of nodes. The applied equations on the *retained nodes* prevent any rigid body motion of the FE model and allow the displacement to be enforced along the y direction while, at the same time, the periodic displacement field on the nodes is ensured:

$$\begin{cases} v_{x,free} = 0 \\ u_{x,fix/y,fix} = 0 \\ v_{x,fix/y,fix} = 0 \\ (w_{x,free} - w_{x,fix/y,fix}) = 0 \end{cases} \quad \begin{cases} u_{y,free} = 0 \\ v_{y,free} = \Delta L \end{cases} \quad \begin{cases} (u_{z,free} - u_{z,fix}) = 0 \\ (v_{z,free} - v_{z,fix}) = 0 \\ w_{z,fix} = 0 \end{cases} \tag{14}$$

The imposed equations on the *face nodes* are equal to the Eqs. (13), where the macroscopic strains are replaced with the displacements of the retained nodes x,*free*, y,*free* and z,*free*:

$$\begin{cases} (u_{x+} - u_{x-}) + u_{x,free} = 0 \\ (v_{x+} - v_{x-}) = 0 \\ (w_{x+} - w_{x-}) = 0 \end{cases} \quad \begin{cases} (u_{y+} - u_{y-}) = 0 \\ (v_{y+} - v_{y-}) - v_{y,free} = 0 \\ (w_{y+} - w_{y-}) = 0 \end{cases} \quad \begin{cases} (u_{z+} - u_{z-}) = 0 \\ (v_{z+} - v_{z-}) = 0 \\ (w_{z+} - w_{z-}) + w_{z,free} = 0 \end{cases} \tag{15}$$

For example, the first set of equations provide the same displacements v and w for the pairs of nodes on the faces with maximum and minimum x-coordinate values, whereas the displacement u of the nodes on face $x+$ is equal to the one of the counterparts on face $x-$ minus the displacement of the retained node x,*free*.

Finally, the *edge nodes* are constrained with equations similar to Eqs. (15), but avoiding over-constraints:

$$
\begin{cases}
(u_{x+/y+} - u_{x-/y+}) + u_{x,free} = 0 \\
(v_{x+/y+} - v_{x-/y+}) = 0 \\
(w_{x+/y+} - w_{x-/y+}) = 0
\end{cases}
\quad
\begin{cases}
(u_{x-/y+} - u_{x-/y-}) = 0 \\
(v_{x-/y+} - v_{x-/y-}) - v_{y,free} = 0 \\
(w_{x-/y+} - w_{x-/y-}) = 0
\end{cases}
\quad
\begin{cases}
(u_{x-/y-} - u_{x+/y-}) - u_{x,free} = 0 \\
(v_{x-/y-} - v_{x+/y-}) = 0 \\
(w_{x-/y-} - w_{x+/y-}) = 0
\end{cases}
$$

$$
\begin{cases}
(u_{x+/z+} - u_{x-/z+}) + u_{x,free} = 0 \\
(v_{x+/z+} - v_{x-/z+}) = 0 \\
(w_{x+/z+} - w_{x-/z+}) = 0
\end{cases}
\quad
\begin{cases}
(u_{x-/z+} - u_{x-/z-}) = 0 \\
(v_{x-/z+} - v_{x-/z-}) = 0 \\
(w_{x-/z+} - w_{x-/z-}) + w_{z,free} = 0
\end{cases}
\quad
\begin{cases}
(u_{x-/z-} - u_{x+/z-}) - u_{x,free} = 0 \\
(v_{x-/z-} - v_{x+/z-}) = 0 \\
(w_{x-/z-} - w_{x+/z-}) = 0
\end{cases}
\tag{16}
$$

$$
\begin{cases}
(u_{y+/z+} - u_{y-/z+}) = 0 \\
(v_{y+/z+} - v_{y-/z+}) - v_{y,free} = 0 \\
(w_{y+/z+} - w_{y-/z+}) = 0
\end{cases}
\quad
\begin{cases}
(u_{y-/z+} - u_{y-/z-}) = 0 \\
(v_{y-/z+} - v_{y-/z-}) = 0 \\
(w_{y-/z+} - w_{y-/z-}) + w_{z,free} = 0
\end{cases}
\quad
\begin{cases}
(u_{y-/z-} - u_{y+/z-}) = 0 \\
(v_{y-/z-} - v_{y+/z-}) + v_{y,free} = 0 \\
(w_{y-/z-} - w_{y+/z-}) = 0
\end{cases}
$$

Appendix B. : Error indexes

The absolute percentage error (APE) is evaluated as follows:

$$
\text{APE} = \left| \frac{\sigma_a^{sim} - \sigma_a^{exp}}{\sigma_a^{exp}} \right|
\tag{17}
$$

where σ_a^{exp} and σ_a^{sim} are the experimental and simulated stress amplitude of a given cycle.

The mean absolute percentage error (MAPE) is equal to the sample mean of the APEs evaluated on each i-th cycle:

$$
\text{MAPE} = \frac{100}{l} \sum_{i=1}^{l} \left| \frac{\sigma_{a,i}^{sim} - \sigma_{a,i}^{exp}}{\sigma_{a,i}^{exp}} \right|
\tag{18}
$$

where l is the total number of cycles under investigation.

References

[1] L. Gibson, M. Ashby, Cellular Solids: Structure and Properties. 2nd ed. Cambridge: Cambridge University Press; 1997. https://doi.org/10.1017/CBO9781139878326.

[2] T.A. Schaedler, W.B. Carter, Architected cellular materials, Annu. Rev. Mater. Sci. 46 (2016) 187–210, https://doi.org/10.1146/annurev-matsci-070115-031624.

[3] L.Y. Chen, S.X. Liang, Y. Liu, L.C. Zhang, Additive manufacturing of metallic lattice structures: unconstrained design, accurate fabrication, fascinated performances, and challenges, Mater. Sci. Eng. R. Rep. 146 (2021) 100648, https://doi.org/10.1016/j.mser.2021.100648.

[4] J. Feng, J. Fu, X. Yao, Y. He, Triply periodic minimal surface (TPMS) porous structures: from multi-scale design, precise additive manufacturing to multidisciplinary applications, Int. J. Extreme Manuf. 4 (2) (2022) 022001, https://doi.org/10.1088/2631-7990/ac5be6.

[5] Z. Xu, I. La Mendola, N. Razavi, S. Bagherifard, Additive manufactured triply periodical minimal surface lattice structures with modulated hybrid topology, Eng. Struct. 289 (2023) 116249, https://doi.org/10.1016/j.engstruct.2023.116249.

[6] R. De Biasi, S. Murchio, E. Sbettega, S. Carmignato, V. Luchin, M. Benedetti, Efficient optimization framework for L-PBF fatigue enhanced Ti6Al4V lattice component, Mater. Des. 230 (2023) 111975, https://doi.org/10.1016/j.matdes.2023.111975.

[7] E. Wang, R. Yao, Q. Li, X. Hu, G. Sun, Lightweight metallic cellular materials: a systematic review on mechanical characteristics and engineering applications, Int. J. Mech. Sci. (2023) 108795, https://doi.org/10.1016/j.ijmecsci.2023.108795.

[8] F. Rosa, S. Manzoni, R. Casati, Damping behavior of 316L lattice structures produced by selective laser melting, Mater. Des. 160 (2018) 1010–1018, https://doi.org/10.1016/j.matdes.2018.10.035.

[9] M. Gavazzoni, S. Beretta, L. Boniotti, E. Di Carmine, L. Gallazzi, R. Iazurlo, S. Foletti, Structural assessment of a multi-functional additively manufactured space component with bulk-lattice hybrid architecture, Thin Wall Struct. 192 (2023) 111158, https://doi.org/10.1016/j.tws.2023.111158.

[10] E.A.A. Alkebsi, H. Ameddah, T. Outtas, A. Almutawakel, Design of graded lattice structures in turbine blades using topology optimization, Int. J. Comput. Integr. Manuf. 34 (4) (2021) 370–384, https://doi.org/10.1080/0951192X.2021.1872106.

[11] Y. Wang, S. Arabnejad, M. Tanzer, D. Pasini, Hip implant design with three-dimensional porous architecture of optimized graded density, J Mech Design. 140 (2018) 111406, https://doi.org/10.1115/1.4041208.

[12] L. Magerramova, M. Volkov, M. Svinareva, A. Siversky, The use of additive technologies to create lightweight parts for gas turbine engine compressors. In Turbo Expo: Power for Land, Sea, and Air (Vol. 51135, p. V07AT30A004). American Society of Mechanical Engineers, (2018, June). https://doi.org/10.1115/GT2018-75904.

[13] S. Das, F. Di Giuseppe, A. Flores, S. Parate, J. Bangal, A case study: analyzing the structure and optimizing the design of the aero handlebar assembly for the bicycle used in Japan's Olympic games, Engineering Reports. (2023) e12783.

[14] R. Shrestha, J. Simsiriwong, N. Shamsaei, Fatigue behavior of additive manufactured 316L stainless steel parts: effects of layer orientation and surface roughness, Addit. Manuf. 28 (2019) 23–38, https://doi.org/10.1016/j.addma.2019.04.011.

[15] A. Tognan, E. Salvati, Probabilistic defect-based modelling of fatigue strength for incomplete datasets assisted by literature data, Int. J. Fatigue 173 (2023) 107665, https://doi.org/10.1016/j.ijfatigue.2023.107665.

[16] B. Rivolta, R. Gerosa, D. Panzeri, Selective laser melted 316L stainless steel: Influence of surface and inner defects on fatigue behavior, Int. J. Fatigue 172 (2023) 107664, https://doi.org/10.1016/j.ijfatigue.2023.107664.

[17] E. Maleki, S. Bagherifard, M. Guagliano, Correlation of residual stress, hardness and surface roughness with crack initiation and fatigue strength of surface treated additive manufactured AlSi10Mg: experimental and machine learning approaches, J. Mater. Res. Technol. 24 (2023) 3265–3283, https://doi.org/10.1016/j.jmrt.2023.03.193.

[18] M. Benedetti, A. Du Plessis, R.O. Ritchie, M. Dallago, S.M.J. Razavi, F. Berto, Architected cellular materials: a review on their mechanical properties towards fatigue-tolerant design and fabrication, Mater. Sci. Eng. R. Rep. 144 (2021) 100606, https://doi.org/10.1016/j.mser.2021.100606.

[19] K. Refai, C. Brugger, M. Montemurro, N. Saintier, An experimental and numerical study of the high cycle multiaxial fatigue strength of titanium lattice structures produced by Selective Laser Melting (SLM), Int. J. Fatigue 138 (2020) 105623, https://doi.org/10.1016/j.ijfatigue.2020.105623.

[20] A. Burr, T. Persenot, P.T. Doutre, J.Y. Buffiere, P. Lhuissier, G. Martin, R. Dendievel, A numerical framework to predict the fatigue life of lattice structures built by additive manufacturing, Int. J. Fatigue 139 (2020) 105769, https://doi.org/10.1016/j.ijfatigue.2020.105769.

[21] A. Zargarian, M. Esfahanian, J. Kadkhodapour, S. Ziaei-Rad, Numerical simulation of the fatigue behavior of additive manufactured titanium porous lattice structures, Mater. Sci. Eng. C 60 (2016) 339–347, https://doi.org/10.1016/j.msec.2015.11.054.

[22] A. Zargarian, M. Esfahanian, J. Kadkhodapour, S. Ziaei-Rad, D. Zamani, On the fatigue behavior of additive manufactured lattice structures, Theor. Appl. Fract. Mech. 100 (2019) 225–232, https://doi.org/10.1016/j.tafmec.2019.01.012.

[23] S. Raghavendra, M. Dallago, F. Zanini, S. Carmignato, F. Berto, M. Benedetti, A probabilistic average strain energy density approach to assess the fatigue strength of additively manufactured cellular lattice materials, Int. J. Fatigue 172 (2023) 107601, https://doi.org/10.1016/j.ijfatigue.2023.107601.

[24] A. Coluccia, G. De Pasquale, Strain-based method for fatigue failure prediction of additively manufactured lattice structures, Sci. Rep. 13 (1) (2023) 22775, https://doi.org/10.1038/s41598-023-49846-z.

[25] D. Molavitabrizi, A. Ekberg, S.M. Mousavi, Computational model for low cycle fatigue analysis of lattice materials: incorporating theory of critical distance with elastoplastic homogenization, Eur. J. Mech. A Solids 92 (2022) 104480, https://doi.org/10.1016/j.euromechsol.2021.104480.

[26] P. Zhang, D.Z. Zhang, B. Zhong, Constitutive and damage modelling of selective laser melted Ti-6Al-4V lattice structure subjected to low cycle fatigue, Int. J. Fatigue 159 (2022) 106800, https://doi.org/10.1016/j.ijfatigue.2022.106800.

[27] F. Mozafari, I. Temizer, Computational homogenization of fatigue in additively manufactured microlattice structures, Comput. Mech. 71 (2023) 367–384, https://doi.org/10.1007/s00466-022-02243-1.

[28] M. Doroszko, A. Seweryn, Cyclic behaviour modelling of additively manufactured Ti-6Al-4V lattice structures, Int. J. Mech. Sci. 273 (2024) 109219, https://doi.org/10.1016/j.ijmecsci.2024.109219.

[29] M. Pelegatti, F. Scalzo, F. Sordetti, E. Vaglio, M. Magnan, G. Totis, M. Sortino, D. Benasciutti, A. Lanzutti, F. De Bona, E. Salvati, Low cycle fatigue behaviour of cellular materials: experimental comparative study of strut-based and gyroid structures made of additively manufactured 316L steel, Int. J. Fatigue 178 (2024) 108024, https://doi.org/10.1016/j.ijfatigue.2023.108024.

[30] A.H. Schoen, Infinite periodic minimal surfaces without self-intersections. NASA Technical Report TN D-5541. Washington, DC; 1970.

[31] I. Maskery, I.A. Ashcroft, The deformation and elastic anisotropy of a new gyroid-based honeycomb made by laser sintering, Addit. Manuf. 36 (2020) 101548, https://doi.org/10.1016/j.addma.2020.101548.

[32] M.I. Okereke, A.I. Akpoyomare, A virtual framework for prediction of full-field elastic response of unidirectional composites, Comput. Mater. Sci 70 (2013) 82–99, https://doi.org/10.1016/j.commatsci.2012.12.036.

[33] M. Pelegatti, D. Benasciutti, F. De Bona, A. Lanzutti, M. Magnan, J.S. Novak, E. Salvati, F. Sordetti, M. Sortino, G. Totis, E. Vaglio, On the factors influencing the elastoplastic cyclic response and low cycle fatigue failure of AISI 316L steel produced by laser-powder bed fusion, Int. J. Fatigue 165 (2022) 107224, https://doi.org/10.1016/j.ijfatigue.2022.107224.

[34] M. Pelegatti, D. Benasciutti, F. De Bona, A. Lanzutti, J.S. Novak, E. Salvati, Strain-controlled fatigue loading of an additively manufactured AISI 316L steel: cyclic plasticity model and strain–life curve with a comparison to the wrought material, Fatigue Fract. Eng. Mater. Struct. 46 (2023) 2195–2211, https://doi.org/10.1111/ffe.13992.

[35] J.L. Chaboche, Time-independent constitutive theories for cyclic plasticity, Int. J. Plast 2 (1986) 149–188, https://doi.org/10.1016/0749-6419(86)90010-0.

[36] M. Dallago, B. Winiarski, F. Zanini, S. Carmignato, M. Benedetti, On the effect of geometrical imperfections and defects on the fatigue strength of cellular lattice structures additively manufactured via Selective Laser Melting, Int. J. Fatigue 124 (2019) 348–360, https://doi.org/10.1016/j.ijfatigue.2019.03.019.

[37] M. Gavazzoni, M. Pisati, S. Beretta, S. Foletti, Multiaxial static strength of a 3D printed metallic lattice structure exhibiting brittle behavior, Fatigue Fract. Eng. Mater. Struct. 44 (12) (2021) 3499–3516, https://doi.org/10.1111/ffe.13587.

[38] N. Korshunova, G. Alaimo, S.B. Hosseini, M. Carraturo, A. Reali, J. Niiranen, F. Auricchio, E. Rank, S. Kollmannsberger, Image-based numerical characterization and experimental validation of tensile behavior of octet-truss lattice structures, Addit. Manuf. 41 (2021) 101949, https://doi.org/10.1016/j.addma.2021.101949.

[39] D. Molavitabrizi, R. Bengtsson, C. Botero, L.E. Rännar, S.M. Mousavi, Damage-induced failure analysis of additively manufactured lattice materials under uniaxial and multiaxial tension, Int. J. Solids Struct. 252 (2022) 111783, https://doi.org/10.1016/j.ijsolstr.2022.111783.

[40] S. Van Bael, G. Kerckhofs, M. Moesen, G. Pyka, J. Schrooten, J.P. Kruth, Micro-CT-based improvement of geometrical and mechanical controllability of selective laser melted Ti6Al4V porous structures, Mater. Sci. Eng. A 528 (2011) 7423–7431, https://doi.org/10.1016/j.msea.2011.06.045.

[41] M. Leary, M. Mazur, H. Williams, E. Yang, A. Alghamdi, B. Lozanovski, X. Zhang, D. Shidid, L. Farahbod-Sternahl, G. Witt, I. Kelbassa, P. Choong, M. Qian, M. Brandt, Inconel 625 lattice structures manufactured by selective laser melting (SLM): mechanical properties, deformation and failure modes, Mater. Des. 157 (2018) 179–199, https://doi.org/10.1016/j.matdes.2018.06.010.

[42] C. Yan, L. Hao, A. Hussein, P. Young, D. Raymont, Advanced lightweight 316L stainless steel cellular lattice structures fabricated via selective laser melting, Mater. Des. 55 (2014) 533–541, https://doi.org/10.1016/j.matdes.2013.10.027.

[43] X. Yang, Q. Yang, Y. Shi, L. Yang, S. Wu, C. Yan, Y. Shi, Effect of volume fraction and unit cell size on manufacturability and compressive behaviors of Ni-Ti triply periodic minimal surface lattices, Addit. Manuf. 54 (2022) 102737, https://doi.org/10.1016/j.addma.2022.102737.

[44] O. Al-Ketan, R. Rowshan, R.K.A. Al-Rub, Topology-mechanical property relationship of 3D printed strut, skeletal, and sheet based periodic metallic cellular materials, Addit. Manuf. 19 (2018) 167–183, https://doi.org/10.1016/j.addma.2017.12.006.

[45] J.S. Armstrong, F. Collopy, Error measures for generalizing about forecasting methods: empirical comparisons, Int. J. Forecast. 8 (1992) 69–80, https://doi.org/10.1016/0169-2070(92)90008-W.

[46] S. Tsopanos, R.A.W. Mines, S. McKown, Y. Shen, W.J. Cantwell, W. Brooks, C.J. Sutcliffe, The Influence of Processing Parameters on the Mechanical Properties of Selectively Laser Melted Stainless Steel Microlattice Structures. (2010), https://doi.org/10.1115/1.4001743.

[47] L. Boniotti, S. Beretta, L. Patriarca, L. Rigoni, S. Foletti, Experimental and numerical investigation on compressive fatigue strength of lattice structures of AlSi7Mg manufactured by SLM, Int. J. Fatigue 128 (2019) 105181, https://doi.org/10.1016/j.ijfatigue.2019.06.041.

[48] A.M. Roach, B.C. White, A. Garland, B.H. Jared, J.D. Carroll, B.L. Boyce, Size-dependent stochastic tensile properties in additively manufactured 316L stainless steel, Addit. Manuf. 32 (2020) 101090, https://doi.org/10.1016/j.addma.2020.101090.

[49] U. Hossain, S. Ghouse, K. Nai, J.R. Jeffers, Mechanical and morphological properties of additively manufactured SS316L and Ti6Al4V micro-struts as a function of build angle, Addit. Manuf. 46 (2021) 102050, https://doi.org/10.1016/j.addma.2021.102050.

[50] P. Magarò, G. Alaimo, M. Carraturo, E. Sgambitterra, C. Maletta, A novel methodology for the prediction of the stress–strain response of laser powder bed fusion lattice structure based on a multi-scale approach, Mater. Sci. Eng. A 863 (2023) 144526, https://doi.org/10.1016/j.msea.2022.144526.

[51] K. Golos, F. Ellyin, A total strain energy density theory for cumulative damage, J. Press. Vessel. Technol. 110 (1988) 36–41, https://doi.org/10.1115/1.3265565.

[52] F. Ellyin, K. Golos, Multiaxial fatigue damage criterion, J. Eng. Mater. Technol. 110 (1) (1988) 63–68, https://doi.org/10.1115/1.3226012.

[53] F. Ellyin, Fatigue damage, crack growth and life prediction, Springer Science & Business Media (2012), https://doi.org/10.1007/978-94-009-1509-1.

[54] P. Lazzarin, R. Zambardi, A finite-volume-energy based approach to predict the static and fatigue behavior of components with sharp V-shaped notches, Int. J. Fract. 112 (2001) 275–298, https://doi.org/10.1023/A:1013595930617.

[55] P. Lazzarin, R. Zambardi, The equivalent strain energy density approach re-formulated and applied to sharp V-shaped notches under localized and generalized plasticity, Fatigue Fract. Eng. Mater. Struct. 25 (10) (2002) 917–928, https://doi.org/10.1046/j.1460-2695.2002.00543.x.

[56] P. Lazzarin, R. Zambardi, Control volumes and strain energy density under small and large scale yielding due to tension and torsion loading, Fatigue Fract. Eng. Mater. Struct. 31 (1) (2008) 95–107, https://doi.org/10.1111/j.1460-2695.2007.01206.x.

[57] A.R. Torabi, F. Berto, A. Campagnolo, Elastic-plastic fracture analysis of notched Al 7075–T6 plates by means of the local energy combined with the equivalent material concept, Phys. Mesomech. 19 (2016) 204–214, https://doi.org/10.1134/S1029959916020144.

[58] P. Lazzarin, F. Berto, Some expressions for the strain energy in a finite volume surrounding the root of blunt V-notches, Int. J. Fract. 135 (2005) 161–185, https://doi.org/10.1007/s10704-005-3943-6.

[59] M. Benedetti, C. Santus, F. Berto, Inverse determination of the fatigue strain energy density control radius for conventionally and additively manufactured rounded V-notches, Int. J. Fatigue 126 (2019) 306–318, https://doi.org/10.1016/j.ijfatigue.2019.04.040.

[60] D. Radaj, State-of-the-art review on the local strain energy density concept and its relation to the J-integral and peak stress method, Fatigue Fract. Eng. Mater. Struct. 38 (2015) 2–28, https://doi.org/10.1111/ffe.12231.

[61] P. Lazzarin, F. Berto, M. Zappalorto, Rapid calculations of notch stress intensity factors based on averaged strain energy density from coarse meshes: Theoretical bases and applications. Int J Fatigue. 2010;32(10):1559-1567. https://doi.org/10.1016/j.ijfatigue.2010.02.017.

[62] P. Foti, F. Berto, Some useful expressions and a proof of the validity of the volume free procedure for the SED method application, Eng. Fract. Mech. 274 (2022) 108818, https://doi.org/10.1016/j.engfracmech.2022.108818.

[63] F.J. Gómez, M. Elices, F. Berto, P. Lazzarin, Local strain energy to assess the static failure of U-notches in plates under mixed mode loading, Int. J. Fract. 145 (2007) 29–45, https://doi.org/10.1007/s10704-007-9104-3.

[64] S. Lee, J.W. Pegues, N. Shamsaei, Fatigue behavior and modeling for additive manufactured 304L stainless steel: the effect of surface roughness, Int. J. Fatigue 141 (2020) 105856, https://doi.org/10.1016/j.ijfatigue.2020.105856.

[65] S.L. Omairey, P.D. Dunning, S. Sriramula, Development of an ABAQUS plugin tool for periodic RVE homogenisation, Eng. Comput. 35 (2019) 567–577, https://doi.org/10.1007/s00366-018-0616-4.